

## CLOUD CLEARING IN THE WAKE OF SATURN'S GREAT STORM OF 2010 – 2011 AND SUGGESTED NEW CONSTRAINTS ON SATURN'S HE/H<sub>2</sub> RATIO.

L.A. SROMOVSKY<sup>1</sup>, K. H. BAINES<sup>1</sup>, P.M. FRY<sup>1</sup>, AND T. W. MOMARY<sup>2</sup>

<sup>1</sup>Space Science and Engineering Center, University of Wisconsin-Madison, 1225 West Dayton Street, Madison, WI 53706, USA and

<sup>2</sup>Jet Propulsion Laboratory, 4800 Oak Grove Drive, Pasadena, CA 91109, USA

*Journal reference: Icarus 276 (2016) 141-142*

### ABSTRACT

Saturn's Great Storm of 2010 – 2011 produced a planet-encircling wake that slowly transitioned from a region that was mainly dark at 5  $\mu\text{m}$  in February 2011 to a region that was almost entirely bright and remarkably uniform by December of 2012. The uniformity and high emission levels suggested that the entire wake region had been cleared not only of the ammonia clouds that the storm had generated and exposed, but also of any other aerosols that might provide significant blocking of the thermal emission from Saturn's deeper and warmer atmospheric layers. Our analysis of VIMS wake spectra from December 2012 provides no evidence of ammonia ice absorption, but shows that at least one significant cloud layer remained behind: a non-absorbing layer of 3 – 4 optical depths (at 2  $\mu\text{m}$ ) extending from 150 to  $\sim$ 400 mbar. A second layer of absorbing and scattering particles, with less than 1 optical depth and located near 1 bar, is also suggested, but its existence as a model requirement depends on what value of the He/H<sub>2</sub> ratio is assumed. The observations can be fit well with just a single (upper) cloud layer for a He/H<sub>2</sub> ratio  $\approx$ 0.064 in combination with a PH<sub>3</sub> deep volume mixing ratio of 5 ppm. At lower He/H<sub>2</sub> ratios, the observed spectra can be modeled without particles in this region. At higher ratios, in order to fit the brightest wake spectrum, models must include either significant cloud opacity in this region, or significantly increased absorption by PH<sub>3</sub>, NH<sub>3</sub>, and AsH<sub>3</sub>. As the exceptional horizontal uniformity in the late wake is most easily understood as a complete removal of a deep cloud layer, and after considering independent constraints on trace gas mixing ratios, we conclude that the existence of this remarkable wake uniformity is most consistent with a He/H<sub>2</sub> mixing ratio of  $0.055^{+0.010}_{-0.015}$ , which is on the low side of the 0.038 – 0.135 range of previous estimates.

*Subject headings:* : Saturn; Saturn, Atmosphere; Saturn, Clouds

### 1. INTRODUCTION

Saturn's Great Storm of 2010 – 2011 was one of the most powerful convective events ever witnessed. Its rapid development, its huge horizontal scale, and the planet encircling wake it generated within  $\sim$ 6 months were accompanied by a prolific generation of lightning (Fischer et al. 2011; Dyudina et al. 2013) and an unusual spectral character consistent with the delivery of ammonia and water ices to the visible cloud deck (Sromovsky et al. 2013), which is  $\sim$ 200 km above the water vapor condensation level near 20 bar, where the lightning also appears to have originated. The dramatic growth of the storm after its initial formation in early December 2010 was documented by amateur and professional groundbased imaging (Sánchez-Lavega et al. 2012) and by Cassini imaging with the Imaging Science Subsystem (ISS) (Sayanagi et al. 2013).

The morphological characteristics of the storm during February and May of 2011 are illustrated in Fig. 1, where ISS images are displayed in comparison with infrared images obtained by the Visual and Infrared Mapping Spectrometer (VIMS). The first VIMS spectral imaging of the storm occurred in February 2011, after it was well developed and had a planet-encircling wake, though at the latitude of the storm head, the region upstream of the head was still undisturbed at that time. In these VIMS images, color assignments are 4.08  $\mu\text{m}$  for red, 1.89  $\mu\text{m}$  for green, and 3.05  $\mu\text{m}$  for blue. The strong absorption at 3  $\mu\text{m}$  in clouds that are bright at the other two wavelengths produce the orange color that indicates the presence of ammonia ice, which was mainly confined to a 10° band of latitude centered at 35°N planetocentric latitude, and much less evident in the secondary wake extending south of

the storm, especially in the May 2011 images.

The sample VIMS data set provided in Fig. 2 emphasizes the most striking spectral characteristic of the storm: its remarkably low reflectivity at wavelengths near 3  $\mu\text{m}$ . (Here brightness is expressed in units of I/F, given by radiance/(solar irradiance/ $\pi$ ), which can exceed unity near 5  $\mu\text{m}$  because there Saturn's thermal emission can exceed the amount of reflected sunlight.) Clearly, the materials convected upward from deeper levels are very different from the surrounding clouds that usually dominate Saturn, which have no trace of 3- $\mu\text{m}$  absorption. From a spectral analysis of the storm head Sromovsky et al. (2013) showed that it contained a mixture of primarily ammonia ice, with likely contributions of water ice, and a third component that might be either NH<sub>4</sub>SH or the unknown material that dominates the upper haze over most of Saturn. As evident in Fig. 1, the ammonia absorption was widespread in the main wake region when the storm head was in a highly active state. We can also see that at 4.08  $\mu\text{m}$ , a pseudo continuum wavelength, the storm clouds are brighter than surrounding clouds, indicating relatively larger particles. Where they are bright at 4  $\mu\text{m}$ , they are also optically thick enough and absorbing enough at 5  $\mu\text{m}$  to block thermal emission from deeper layers of Saturn's atmosphere. The wake region in February 2011 also had regions where 5- $\mu\text{m}$  emission was greater than regions upstream of the storm, one of which (near 150° east) is near the long-lived anticyclonic vortex (AV) described by Sayanagi et al. (2013) and Momary and Baines (2014) and may be an effect produced by that circulation feature.

Figure 2 also shows that a remarkable transition of the wake

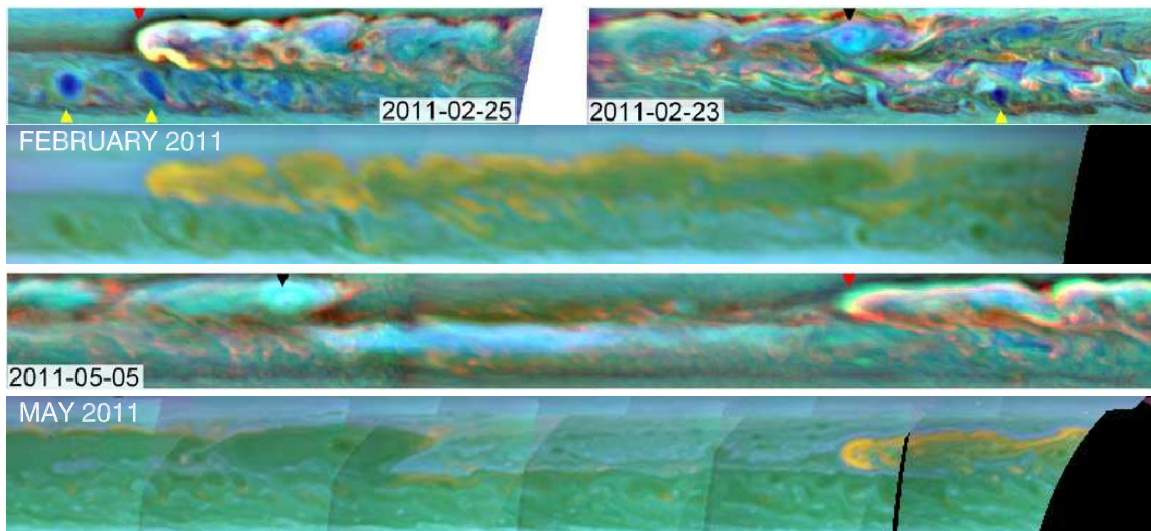


FIG. 1.— Early stages of the Great Storm in February 2011 (top 2 panels). The first and third panels from the top, from Sayanagi et al. (2013), are mosaics of ISS observations displayed using CB2, MT2, and MT3 filters for R, G, and B channels, in which red triangles indicate the location of the storm head, black triangles the location of the large bright blue anticyclonic oval vortex, which Sayanagi et al. referred to as the AV, and yellow triangles the locations of dark ovals. The storm head disappeared after it caught up to the anticyclone in June 2011. The second and fourth panels are from VIMS, covering  $200^\circ$  of longitude and latitudes  $20^\circ$  N to  $44^\circ$  N. The VIMS color maps used  $R = 4.08 \mu\text{m}$ ,  $G = 1.89 \mu\text{m}$ , and  $B = 3.05 \mu\text{m}$ , for which yellow/orange regions indicate large particles, optically thick clouds, and strong  $3\text{-}\mu\text{m}$  absorption characteristic of ammonia ice. Note that features may appear at slightly different longitudes in pairs of maps from the same month due to time differences.

region occurred during the the two years following its beginning in early December 2010. By December 2012, in the latitude band from  $30^\circ$  N to  $39^\circ$  N there was no evidence of bright large-particle cloud features at  $4.08 \mu\text{m}$  and no evidence of  $3\text{-}\mu\text{m}$  absorption by ammonia ice (or anything else). Most surprising, and a unique outer planet feature as far as we know, the primary wake region turned from being mainly very dark at  $5 \mu\text{m}$  to being entirely bright and remarkably uniform. This indicates a dramatic decrease in the opacity of aerosols that normally attenuate thermal radiation emanating from the  $5 - 6$  bar level in Saturn’s atmosphere. I/F values at  $5 \mu\text{m}$  increased from pre-storm values of  $0.6 - 0.8$ , and even lower deep storm values of  $0.2 - 0.3$ , to a remarkably high I/F averaging  $\sim 2.7$ . The spatial uniformity and high emission levels reached by December 2012 suggested that the entire wake region had been cleared not only of the ammonia clouds that the storm had generated, but also of any other deep aerosols that might provide significant blocking of Saturn’s  $5\text{-}\mu\text{m}$  thermal emission.

In the following, we use VIMS imaging at  $5 \mu\text{m}$  to define the morphological evolution of the wake’s “cleared” regions. We then use VIMS spectral observations to constrain the cloud structure of those regions, finding that they were not completely cleared of all aerosols, but instead retained an upper level cloud similar to surrounding regions. We show that a deep layer of aerosols that blocks part of the thermal emission declined dramatically to less than one optical depth, and is only needed if the He/H<sub>2</sub> mixing ratio is at the higher end of the range of values previously published, but find that complete deep clearing could explain the remarkable uniformity of the late wake region if the He/H<sub>2</sub> mixing ratio is in the lower part of that range.

## 2. OVERVIEW OF WAKE EVOLUTION

### 2.1. Evolution of apparent wake “clearing”

The morphological evolution of the wake is illustrated by the  $5\text{-}\mu\text{m}$  mosaics displayed in Fig. 3. After the anticyclone was overtaken by the head of the storm in mid June 2011

(Sayanagi et al. 2013), no evidence of the storm head was subsequently seen. But even before that event, the wake was already beginning to develop regions of high emission at  $5 \mu\text{m}$ , evident from the 11 May 2011 mosaic in Fig. 3. It may also be significant that the region around the anticyclone (near  $320^\circ\text{E}$  in that mosaic) is marked by excess emission. The widespread clearing seemed to begin in local regions distributed near the mid line of the storm’s main wake, and over time became more widely distributed within the wake. By August 2011, the regions of excess  $5\text{-}\mu\text{m}$  emission grew significantly in number and both in longitudinal coverage and in latitudinal extent. By December 2012 the  $5\text{-}\mu\text{m}$  bright wake region spanned latitudes from  $30^\circ$  N to  $39^\circ$  N (planetocentric), extended over all longitudes, and became nearly uniform in brightness, suggesting the possibility of complete removal of the cloud layer that was strongly attenuating thermal emissions from the deeper layers of Saturn. However, we will show in what follows that the cloud clearing explanation is only plausible for a limited range of He/H<sub>2</sub> mixing ratios.

### 2.2. Development of spatial uniformity in the cleared wake region

A quantitative measure of the developing spatial uniformity of the wake region is provided by longitudinal scans at  $35^\circ$  N for each of the mosaics displayed in Fig. 3. These scans show that I/F values at  $5.12 \mu\text{m}$  (as corrected for view angle variations) were  $\sim 1.0$  upwind of the storm head in February 2011, but ranged from  $0.3$  to  $1.9$  downstream of the storm head, with relatively small variability ahead of the storm and much larger variability in the wake region. The wake variability at this wavelength increased dramatically by May 2011, both in amplitude of variation (ranging from  $\sim 0.2$  to  $\sim 2.7$ ) and in spatial frequency. But by January 2012, as the wake extended over most longitudes, the I/F in the wake region grew much more uniform, with most values between  $2.4$  and  $2.6$ . Finally, by December of 2012, the mean wake I/F reached  $2.75$  with a standard deviation of only  $2\%$ . A plausible qualitative explanation of this behavior is that the tropospheric temperature structure remained relatively stable both longitudinally and

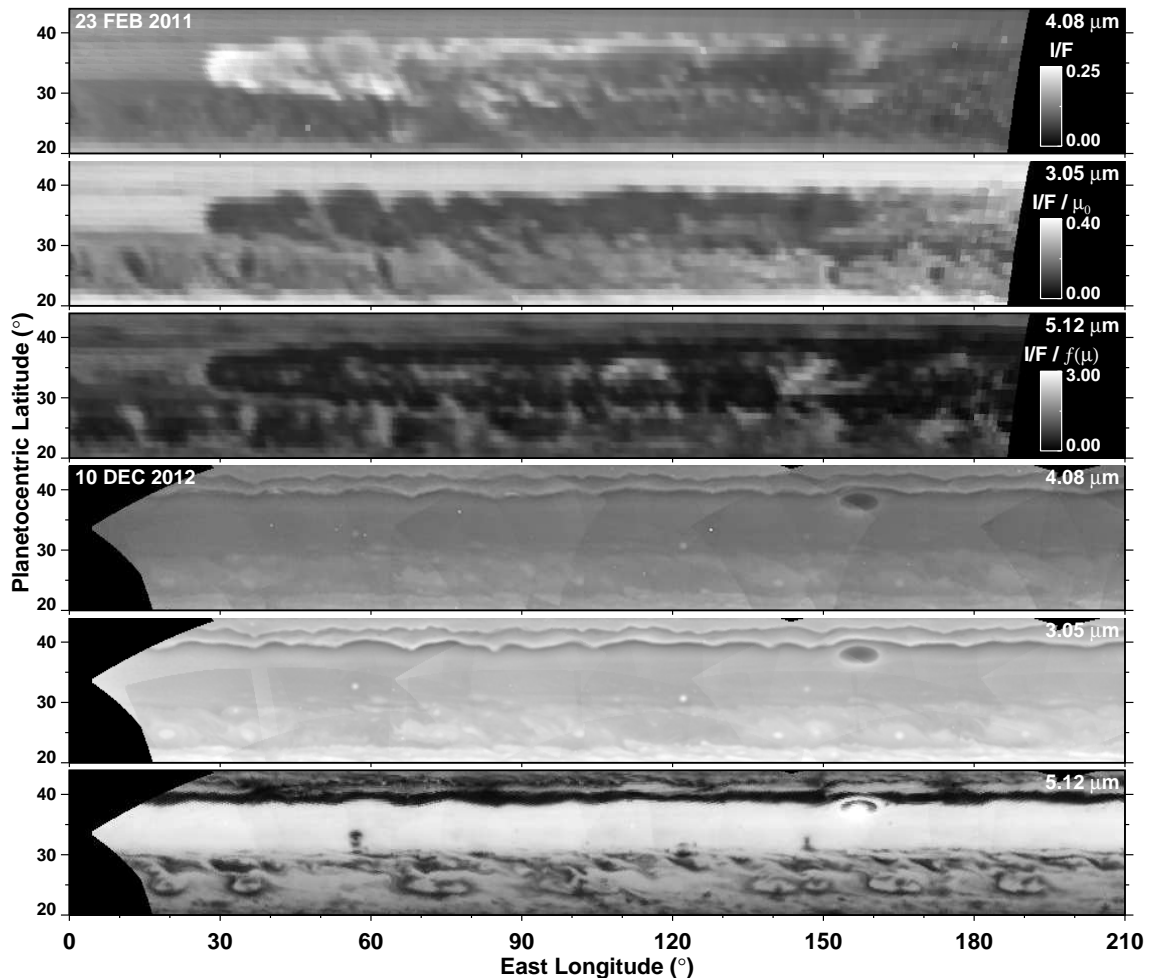


FIG. 2.— Comparison of storm latitudes at 3.05, 4.08, and 5.12  $\mu\text{m}$ , on 23 February 2011 (top three panels) and 10 December 2012 (bottom three panels). In the 23 February 2011 images, we see that clouds with large particles, indicated by features that are bright at 4.08  $\mu\text{m}$ , are also clouds with a significant ammonia ice component, indicated by absorption at 3.05  $\mu\text{m}$ , and are optically thick enough (and absorbing enough) to block thermal emission at 5  $\mu\text{m}$ . On the other hand, in the 10 December 2012 images there is no evidence of large particles, no evidence of ammonia absorption, and a surprisingly uniform lack of blocking of 5- $\mu\text{m}$  thermal emission. The gray scales used for the bottom three panels are the same as for the corresponding top three panels. Mosaics were blended with approximate limb darkening corrections: at 3.05  $\mu\text{m}$  I/F values were divided by the cosine of the solar zenith angle; at 5.12  $\mu\text{m}$  I/F values were divided by  $f(\mu) = 0.427 - 0.445\mu + 1.019\mu^2$ , where  $\mu$  is the cosine of the observer zenith angle; no correction was made at 4.08  $\mu\text{m}$ .

over time, but that the deep ammonia cloud layer present before the storm became disturbed by heterogeneous convective towers during the storm, leading to reduced emission where clouds were developing and increased emission where local downwelling motions produced a reduction in deep cloud optical depth. This perhaps led to strong variability while the storm clouds were active. But after the storm subsided, the deep clouds were completely cleared, perhaps by the mechanism of Li and Ingersoll (2015). Whether this interpretation is quantitatively consistent with cloud structure inferred by radiative transfer modeling is treated in a subsequent section. The fact that the peak I/F seen in May 2012 is essentially the same as the mean seen in the December 2012 mosaic suggests that the main difference between them is the fraction of cloud clearing rather than changes in thermal structure.

### 3. OVERVIEW OF VIMS SPECTRAL OBSERVATIONS

#### 3.1. Observations list

Our work is based on VIMS observations gathered from February 2011 (the first VIMS observations of the storm region) through December 2012 (when the cleared region reached full longitudinal and latitudinal extent). Data sets that

were analyzed and observing conditions are listed in Table 1. These all include measurements of reflected sunlight as well as thermal emission, which we found to provide the best combination of constraints on upper and lower cloud parameters and  $\text{PH}_3$ .

#### 3.2. VIMS instrumental characteristics

VIMS is a 2-channel mapping spectrometer, one channel covering the 0.35 – 1.0  $\mu\text{m}$  spectral range, and the second covering an overlapping near-IR range from 0.85 – 5.1  $\mu\text{m}$ . The near-IR spectral range is covered by 256 contiguous wavelength bands sampled at a nominal interval of 0.016  $\mu\text{m}$ . Each spatial sample (pixel) has a square field of view 0.5 milliradians on a side, and a typical image frame has dimensions of 64 pixels by 64 pixels. Detailed descriptions of the VIMS instrument are provided by Brown et al. (2004) and McCord et al. (2004). All wavelengths are measured simultaneously. Spatial samples are obtained via raster scans of the instrument field of view across the target. Random noise is a very small contributor to uncertainty in the VIMS observations. It is systematic effects that are the main source of uncertainties in deriving atmospheric constraints from the VIMS spectra. Many

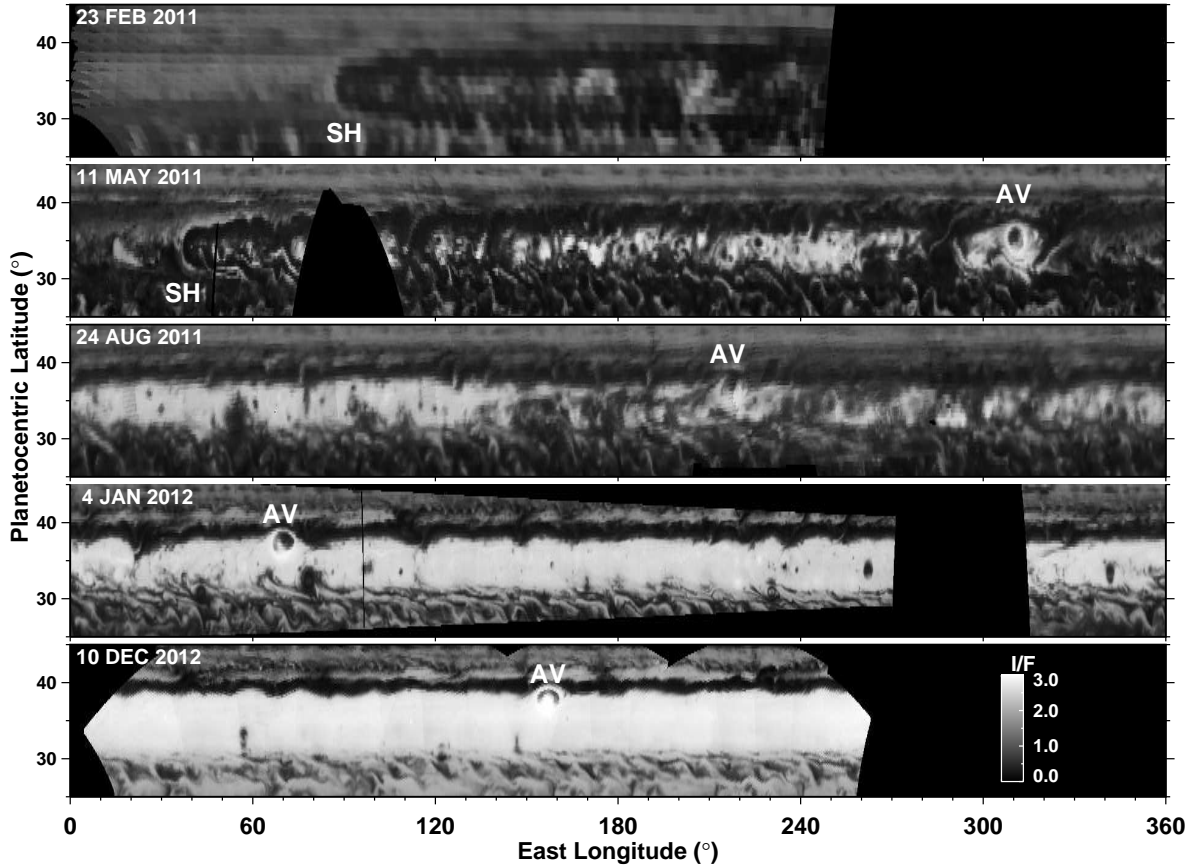


FIG. 3.— Rectilinear  $5\text{-}\mu\text{m}$  maps showing the evolution of apparent wake-clearing from 23 February 2011 to 10 December 2012. All images are shown with the same gray scale indicated for the December 2012 image. For easier comparison with wake structure in May, the February map was displayed  $160^\circ$  west of its actual position. In four of the images we marked the position of the anticyclonic vortex (AV) that developed along with the Great Storm. The storm head (SH) is marked in the top two images, but not in subsequent images because it dissipated after encountering the AV in mid June.

TABLE 1  
LIST OF RC17-CALIBRATED VIMS DATA CUBES AND OBSERVING CONDITIONS USED IN OUR ANALYSIS.

Observation ID	Cube Version	UT Date YYYY-MM-DD	Start Time	Pixel size	Phase angle
VIMS_145SA_WIND5HR001	V1677201862_3	2011-02-24	00:36:35	882 km	$51^\circ$
VIMS_148SA_NHEMMAP001_PRIME	V1683829310_1	2011-05-11	17:33:22	331 km	$23^\circ$
VIMS_152SA_PEARLMOV001_PRIME	V1692862427_1	2011-08-24	06:44:21	403 km	$15^\circ$
VIMS_159SA_HIRESMAP001_PRIME	V1704401716_1	2012-01-04	20:04:37	157 km	$56^\circ$
VIMS_160SA_MIRMAP001	V1705983395_1	2012-01-23	03:25:46	1137 km	$74^\circ$
VIMS_176SA_NORSTRM001_PRIME	V1733862483_1	2012-10-12	19:34:16	274 km	$36^\circ$
VIMS_176SA_NORSTRM001_PRIME	V1733869346_1	2012-12-10	21:28:39	288 km	$31^\circ$

are related to calibration uncertainties.

### 3.3. VIMS calibration

There are four aspects of the VIMS calibration that merit special attention. First, is the wavelength scale and its variation over time. Sromovsky et al. (2013) noted that the wavelengths of the VIMS spectral channels had changed typically by 5 – 10 nm relative to the assignments given in data headers. Here we used a scaled version of the shifts given by Sromovsky et al. (2013). These were based on alignment of atmospheric gas absorption features with well known wavelengths. A second aspect is the correction for responsivity depressions in the vicinity of the joints in order sorting filters on the VIMS detector array, which occur near wavelengths of  $1.69\ \mu\text{m}$ ,  $2.98\ \mu\text{m}$ , and  $3.85\ \mu\text{m}$  (Miller et al. 1996; Brown et al. 2004). The smallest effect on responsivity is

at the  $2.98\text{-}\mu\text{m}$  joint, which can be corrected for following Sromovsky et al. (2013). Effects at the other two joints are much larger and not reliably correctable, and thus not used in constraining model cloud structures. A minor aspect is the correction of nominal exposures for clock rate and time offset. From comparison of images of Jupiter at exposures of 20 ms, 80 ms, and 160 ms, we found that the previous rule in which  $T(\text{corrected}) = T(\text{nominal}) \times 1.0175 - 4\ \text{ms}$  needed to be changed to the  $T(\text{corrected}) = T(\text{nominal}) \times 1.0175 - 1.67\ \text{ms}$ . Without the change, I/F values computed for 60 ms exposures are about 10% too large. As most exposures are much longer, this is not generally an important correction. The fourth issue has to do with the radiometric calibration, which has been updated several times over the years. Clark et al. (2012) described a new radiometric calibration, termed RC17, which was released to PDS and ISIS3 in mid 2014. That is the ra-

diometric calibration used in our current analysis. Flat-field correction files have also been revised over time. In this analysis we used the 2009 flat named `ir_flat_3_2009.cub` in PDS volumes and `ir_flatfield_v0002.cub` in ISIS3. The ISIS system is described by Anderson et al. (2004).

#### 4. RADIATIVE TRANSFER MODELING

Our radiative transfer calculations follow essentially the approach used by Sromovsky et al. (2013), using the same multiple scattering code that simultaneously accounts for thermal emission and reflected sunlight. A revision of the code has enhanced its ability to use parallel processing to speed calculations. While the prior code did each of the ten correlated-k terms in parallel, the revision allows multiple wavelengths to be run in parallel as well. A second exception is that we treated the thermal profile differently, as described in a following section. A third exception is how we handled line-spread functions, which is also described in a separate section. Here we summarize our assumed composition and gas absorption models.

##### 4.1. Atmospheric composition

Measured by their effects on Saturn's 1 – 5  $\mu\text{m}$  spectrum, the most important minor gases are methane ( $\text{CH}_4$  and  $\text{CH}_3\text{D}$ ), phosphine ( $\text{PH}_3$ ), arsine ( $\text{AsH}_3$ ), and ammonia ( $\text{NH}_3$ ). In reflected sunlight ( $\lambda < 4.6 \mu\text{m}$ ), methane and phosphine are dominant, while in thermal emission ( $\lambda > 4.6 \mu\text{m}$ ) phosphine is dominant, with arsine and ammonia playing relatively minor roles. For  $\text{CH}_4$  we used the Fletcher et al. (2009b) volume mixing ratio of  $(4.7 \pm 0.2) \times 10^{-3}$ , which corresponds to a  $\text{CH}_4/\text{H}_2$  ratio of  $(5.3 \pm 0.2) \times 10^{-3}$ . For  $\text{CH}_3\text{D}$  we also used the Fletcher et al. (2009b) VMR value of  $3 \times 10^{-7}$ . The most important variable gas is  $\text{PH}_3$ , and its vertical profile needs to be adjusted to fit VIMS spectra. We followed Fletcher et al. (2009a) in defining a pressure break point  $P_0$ , below which (in altitude) the mixing ratio is a constant  $\alpha_0$  and above which the mixing ratio falls off with a constant gas to pressure scale height ratio  $f$ , so that the mixing ratio as a function of pressure can be written as

$$\alpha(P) = \alpha_0(P/P_0)^{(1-f)/f} \quad \text{for } P < P_0. \quad (1)$$

For profiles with an additional break point at  $P_1 < P_0$  we can write the mixing ratio above that point as

$$\alpha(P) = \alpha_0(P_1/P_0)^{(1-f)/f} (P/P_1)^{(1-f_1)/f_1} \quad \text{for } P < P_1$$

with Eq. 1 still applying for  $P_1 < P < P_0$ . In most cases we used profiles with a single break point with scale height ratios near 0.5, somewhat greater than the CIRS-based values of Fletcher et al. (2009a) and much greater than values near 0.2 typical of the Fletcher et al. (2011) results at comparable latitudes. For our initial calculations we used a break point at  $P_0 = 550 \text{ mb}$  and deep mixing ratios of 4 – 5 ppm, which are comparable to the CIRS-based values. We also assumed an initial  $\text{He}/\text{H}_2$  ratio of 0.0638 (Hanel et al. 1981), a constant  $\text{AsH}_3$  volume mixing ratio of 6 ppb, and the  $\text{NH}_3$  profile given by Prinn et al. (1984), which has a constant deep mixing ratio of  $2.05 \times 10^{-4}$ , based on Courtin et al. (1984).

##### 4.2. Gas absorption models

We limited our analysis to  $\lambda > 1.268 \mu\text{m}$  so that correlated-k models for methane absorption could be based on line-by-line calculations, following Sromovsky et al. (2012). We used the same line data for computing  $\text{CH}_3\text{D}$  absorption models.

For  $\text{NH}_3$  we used the combined correlated-k absorption model described by Sromovsky and Fry (2010), which is based primarily on the Goody-Lorentz band model of Bowles et al. (2008). Our exponential sum approximations of phosphine ( $\text{PH}_3$ ) absorption are based on the line data of Butler et al. (2006) in the 2.8 – 3.1  $\mu\text{m}$  region and on the Rothman et al. (2009) HITRAN 2008 line data in the 4.1 – 5.1  $\mu\text{m}$  region. Our model of  $\text{AsH}_3$  absorption is based on line data from Tarrago (1996) (via G. Bjoraker, via B. Bézard, personal communication). Where multiple gases have overlapping absorptions we followed Lacis and Oinas (1991) to obtain 10-term correlated-k approximations for the combined gases. Collision-induced absorption (CIA) for  $\text{H}_2$  and  $\text{H}_2\text{-He}$  was calculated using programs downloaded from the Atmospheres Node of the Planetary Data System, which are documented by Borysow (1991, 1993) for the  $\text{H}_2\text{-H}_2$  fundamental band, Zheng and Borysow (1995) for the first  $\text{H}_2\text{-H}_2$  overtone band, and by Borysow (1992) for  $\text{H}_2\text{-He}$  bands. The diagnostic value of these gases can be estimated from their penetration depths shown in Fig. 4. Arsine has a noticeable effect on the VIMS spectra at 4.5 – 4.9  $\mu\text{m}$ , which is where ammonia gas also plays a relatively minor role. Ammonia is more important in controlling thermal radiation at wavelengths beyond 5.1  $\mu\text{m}$ .

##### 4.3. Thermal structure and the $\text{He}/\text{H}_2$ ratio

Voyager 2 radio occultation measurements (Tyler et al. 1982) were used to determine refractivity profiles for Saturn. From the refractivity profiles,  $T(P)$  profiles could be constructed for any given assumed molecular composition. The composition providing the best fits to IRIS spectral measurements in the 207  $\text{cm}^{-1}$  – 602  $\text{cm}^{-1}$  spectral range, calculated over a range of latitudes, corresponded to a hydrogen mole fraction of  $0.940 \pm 0.005$  (Hanel et al. 1981), with an additional absorption coefficient uncertainty of  $\pm 0.005$ . Ignoring the minor effects of heavier molecules, this leads to a  $\text{He}/\text{H}_2$  ratio of  $0.0638 \pm 0.007$ , using the root sum of squares of the random and coefficient uncertainties. Using this composition Lindal et al. (1985) derived a  $T(P)$  profile from the Voyager 2 ingress refractivity profile down to about 800 mb, and added trace amounts of  $\text{NH}_3$  to constrain the profile down to 1.3 bars. We extended this profile to 10 bars assuming an adiabatic lapse rate of approximately -0.83 K/km. To accommodate the possibility of other  $\text{He}/\text{H}_2$  ratios, we scaled this profile to preserve the same refractivity profile, using the scaling relations (Conrath and Gautier 2000):

$$T = T_0 \frac{m}{m_0}, \quad P = P_0 \frac{m\alpha_0}{m_0\alpha}, \quad (3)$$

where  $T$ ,  $P$ ,  $m$ , and  $\alpha$  are the temperature, pressure, molecular weight, and refractivity respectively of the modified profile, and the same quantities with a zero subscript are for the original profile. Two sample profiles are shown in Fig. 5A, which also shows how the different profiles effect the pressure at which  $\text{NH}_3$  would become saturated, using sample  $\text{NH}_3$  volume mixing ratios of 200 ppm and 400 ppm. Note that the condensation level moves to lower pressures for higher values of the  $\text{He}/\text{H}_2$  ratio. The reflection and emission spectra of Saturn are both affected by the  $\text{He}/\text{H}_2$  ratio because the collision-induced absorption is dependent on the ratio, but the effect is most dramatic on the thermal emission spectrum because of the strong dependence of radiance on temperature in the 5- $\mu\text{m}$  region, where most of the emitted radiation originates (Fig. 5B). At low values of the  $\text{He}/\text{H}_2$  ratio the atmo-

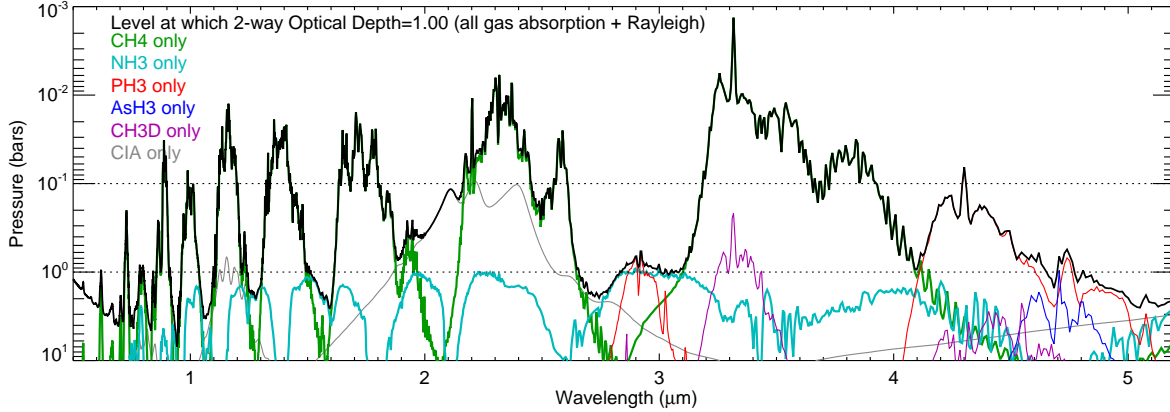


FIG. 4.— Penetration depth of near-IR photons indicated by pressures at which a unit albedo reflecting layer produces an external I/F of  $1/e$  at normal incidence and viewing. Curves are shown for methane only (green), ammonia only (cyan), phosphine only (red), arsine only (purple),  $\text{CH}_3\text{D}$  only (magenta), CIA only (gray), and all gases combined (black), assuming the Lindal et al. (1985) temperature profile, the ammonia profile of Prinn et al. (1984), a  $\text{He}/\text{H}_2$  ratio of 0.0638, a phosphine deep mixing ratio of 5 ppm, falling off above 0.69 bars with a  $\text{PH}_3$  to pressure scale height ratio of 0.5, an  $\text{AsH}_3$  VMR of 6 ppb, and a  $\text{CH}_3\text{D}$  VMR of 0.3 ppm.

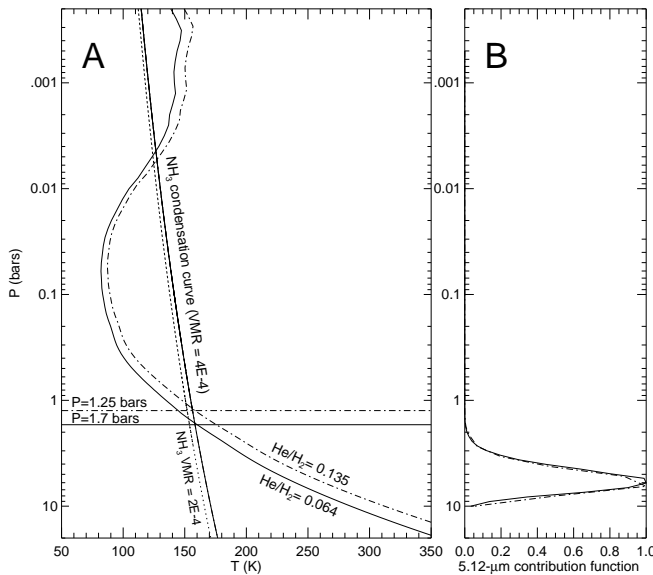


FIG. 5.— A: Temperature profiles for two assumed  $\text{He}/\text{H}_2$  ratios of 0.064 (solid) and 0.135 (dot-dash). Also shown are the  $\text{NH}_3$  saturation vapor pressure profile versus temperature for volume mixing ratios of  $2 \times 10^{-4}$  and  $4 \times 10^{-4}$ , and pressures at which  $\text{NH}_3$  condensation can be expected to occur. B: Contribution functions  $B_\lambda(T) \exp(-\tau) d\tau / d \ln P$  normalized to the peak at  $5.12 \mu\text{m}$  for each temperature profile plotted in A. The peak contributions are from the 5.4 – 5.9 bar level.

sphere becomes cool enough that the observed 5- $\mu\text{m}$  emission cannot be reproduced by even a cloud-free model.

Unfortunately, the  $\text{He}/\text{H}_2$  ratio for Saturn is far from certain, as summarized in Fig. 6. From Pioneer Saturn infrared radiometer measurements combined with Pioneer radio occultation data, Orton and Ingersoll (1980) derived a mole fraction of  $\text{H}_2$  equivalent to  $\text{He}/\text{H}_2 = 0.11 \pm 0.03$ . Using essentially the same method applied to Voyager observations (Hanel et al. 1981) inferred a hydrogen abundance equivalent to  $\text{He}/\text{H}_2 = 0.0638 \pm 0.007$ , while a later Voyager analysis by Conrath et al. (1984) yielded a value of the  $\text{H}_2$  mole fraction equivalent to  $\text{He}/\text{H}_2 = 0.038 \pm 0.026$ . These values derived by radio occultation and thermal spectral comparisons became suspect following the Galileo Probe in situ measurements of  $0.157 \pm 0.003$  for the ratio on Jupiter (von Zahn et al. 1998;

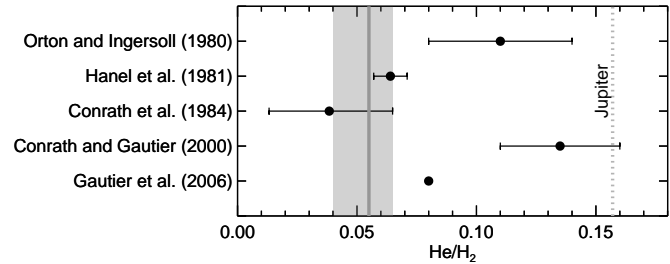


FIG. 6.— Estimates of the  $\text{He}/\text{H}_2$  ratio on Saturn using methods described in the text. The value for Jupiter (dotted line) is  $0.157 \pm 0.003$  (von Zahn et al. 1998). The range most consistent with cloud clearing is shown by the gray band.

Niemann et al. 1998), which is  $1.6 \times \sigma$  larger than the Voyager inferred value for Jupiter of  $0.11 \pm 0.03$  (Gautier et al. 1981). To avoid whatever systematic errors that might be affecting the occultation-thermal spectral method, Conrath and Gautier (2000) derived the ratio from IRIS spectra alone, resulting in a value of  $0.135 \pm 0.024$ . More recent results using Cassini radio occultations in combination with Cassini CIRS spectra, by Gautier et al. (2006), have yielded a value near 0.08 according to Fouchet et al. (2009), although no specific value (or uncertainty) appears in the Gautier et al. (2006) abstract. We will later show that if uniformity of the late wake region is to be explained by the absence of deep aerosols, the  $\text{He}/\text{H}_2$  ratio needs to be in the range depicted by the gray bar in Fig. 6, which is within the lower range of values previously determined.

#### 4.4. Estimating uncertainties in derived model parameters

Uncertainty estimates in derived model parameters depend critically on estimates of the instrumental and gas absorption model errors, neither of which is very well understood. Random errors in the VIMS measurements are only a minor contributor except at very low signal levels. Much more important are systematic effects arising from instrument calibration errors, wavelength scale errors, and uncertainty in gas and particulate absorption models. For example, we have seen VIMS calibration changes over the years by as much as 20% in the 3- $\mu\text{m}$  region of the spectrum and by similar amounts due to differences in flat field corrections. Presumably current calibration errors have been reduced over time, but un-

certainty estimates for the current calibrations are not well defined. Wavelength scale changes have already been noted in a previous section, and there is some uncertainty associated with attempts to correct for the known wavelength shifts.

Following Sromovsky et al. (2013), we tried to account for these various effects in a semi-realistic way using the following procedure. Initial model fits were used to establish a rough characterization of the vertical opacity structure of the atmosphere. Model spectra were then calculated for the rough model, and for two perturbations: (1) optical depths offset by 0.01 and (2) optical depths increased by 10%. The resulting I/F differences were then root sum squared with I/F errors due to wavelength uncertainties, and with an I/F offset uncertainty of  $5 \times 10^{-4}$  and a measurement/relative calibration uncertainty assumed to be 1%. The I/F error associated with wavelength uncertainty was calculated from the derivative of the I/F spectrum with respect to wavelength times an estimated wavelength uncertainty of  $0.002 \mu\text{m}$ , which is 1/8 of a VIMS line width. An alternative and simpler model computed I/F error as the root sum of squares of an offset error of 0.005 in I/F and a fractional signal error of 6%. The second model led to roughly the same fit characteristics as the first on test cases. Thus we used the simpler model in most calculations. For comparison we note that Fletcher et al. (2011) used a much more conservative error model for VIMS thermal spectra, consisting of the greater of 12% of radiance or 12% of mean radiance over the  $4.6 - 5.1 \mu\text{m}$ . Our model results in smaller error predictions, yet in most cases we are able to achieve fits with  $\chi^2$  values between 1 and 2 times the number of degrees of freedom ( $N_F = \text{number of fitted points minus the number of fitted parameters}$ ). To approximately correct for bad error estimates and incomplete physics, we re-scaled our  $\chi^2$  values by the factor  $N_F/\chi_{MIN}^2$  before finding confidence limits.

## 5. SPECTRALLY CONSTRAINED CLOUD STRUCTURE

We are able to accurately model the VIMS spectra with a relatively simple cloud structure consisting of two main cloud layers. The top cloud is parameterized as a conservative cloud, using spherical Mie particles with refractive index  $n = 1.4 + 0i$ , a top pressure ( $p2t$ ), a bottom pressure ( $p2$ ), a particle radius ( $r2$ ), and an optical depth ( $od2$ ). We assume a gamma size distribution (Hansen and Travis 1974) with a fixed variance of 0.1. Although these particles are likely not spherical, this choice of spherical particles is a convenient way to parameterize wavelength dependence and is a reasonable approximation for small enough size parameters (Fry and Sromovsky 2014). The bottom cloud is modeled as a sheet cloud of Henyey-Greenstein particles with arbitrarily chosen single scattering albedo of  $\varpi = 0.95$  and asymmetry parameter of  $g = 0$  (these cannot be independently constrained due to the significant optical depth of the overlying cloud). The lower cloud adjustable parameters are its optical depth ( $odm$ ) and pressure ( $pm$ ). We did not attempt to constrain the wavelength dependence of this cloud as it is mainly constrained by its effects in the  $5\text{-}\mu\text{m}$  window. Its inferred optical depth is a strong function of its assumed single-scattering albedo. This arises because its effectiveness at blocking thermal emission is low with a high single-scattering albedo, requiring more optical depth than if the cloud is more absorbing. Because the observations are not sensitive to the thickness of this cloud, we chose the simplification of removing that parameter with the sheet cloud assumption (we made the cloud top pressure  $0.995 \times$  the bottom pressure). There is also an

optically thin haze layer of sub-micron particles (effective radius =  $r1$  with a similar gamma size distribution) at pressure  $p1$  with optical depth  $od1$ . This layer is needed to fit the low but non-zero I/F values in spectral regions with strong gas absorption. For fits including reflected sunlight at modest incidence angles, we find  $r1 = 0.14 \mu\text{m}$  and  $od1 = 0.01 - 0.02$  work well, but these parameters are not of much physical significance because the effect of this layer is at the level of the VIMS offset uncertainty for the observing conditions of our chosen spectral data.

### 5.1. Sensitivity of model spectra to model parameters

The seven adjustable parameters we used are listed in Table 2, along with the parameters that are either fixed or manually altered, but not part of the Levenberg-Marquardt non-linear fitting process. For a pre-storm spectrum at  $35^\circ$  N planetocentric latitude, we show in Fig. 7 the derivative of the model spectrum with respect to each of the normally adjusted parameters. These derivative spectra are distinctly different, although there are some significant correlations between some of the parameters as listed in Table 3. For example, because both  $p2t$  and  $p2$  produce spectrally similar decreases in the I/F spectrum, during the fitting process, these tend to move in opposite directions to maintain a more constant effective pressure for the layer. This correlation could have been suppressed by using an alternate parameterization in which mean pressure and pressure thickness were the adjustable parameters. There are also strong correlations between optical depth and cloud boundaries for layer 2 for reflection spectra. This arises because moving the top pressure upward makes the cloud brighter, which needs to be compensated for by reducing its optical thickness. Similarly, moving the bottom downward makes the cloud darker, requiring a compensating increase in optical depth. None of the correlations have prevented reasonably good constraints on particle parameters, as can be seen from the fit results to follow.

Another important characteristic to take note of in Fig. 7 is that some parameters have vastly more important effects on the part of the spectrum dominated by thermal emission ( $\lambda > 4.5 \mu\text{m}$ ) relative to their effects on the part dominated by reflected sunlight. For example, the derivative with respect to the optical depth of the deeper cloud layer (panel H) has essentially no effect at most solar-dominated wavelengths, with the main exception being near  $2.7 \mu\text{m}$ , where the atmosphere is sufficiently transparent that the light reflected by that deeper cloud makes a small positive contribution. Its effect at thermal wavelengths is negative as a result of the absorption it provides. Another dramatic spectral difference in effects can be seen in panel B, where the derivative with respect to the optical depth of the main upper cloud has only a tiny effect at wavelengths of thermal emission, a result of the conservative nature of the cloud particles.

### 5.2. Fit results for $\text{He}/\text{H}_2 = 0.064$

A sample fit to an upstream spectrum is provided in Fig. 8, with fit parameters, uncertainties, and fit quality provided in the first row of Table 4. This spectrum, from location A in Fig. 9, has a relatively low I/F in the  $4.6 - 5.12 \mu\text{m}$  region and thus the model requires a lower cloud of significant absorption optical depth to limit thermal emission. As can be seen in Fig. 8 from what happens to the model spectrum when the upper cloud is removed, the overlying cloud of conservative particles provides little attenuation. The assumed lower

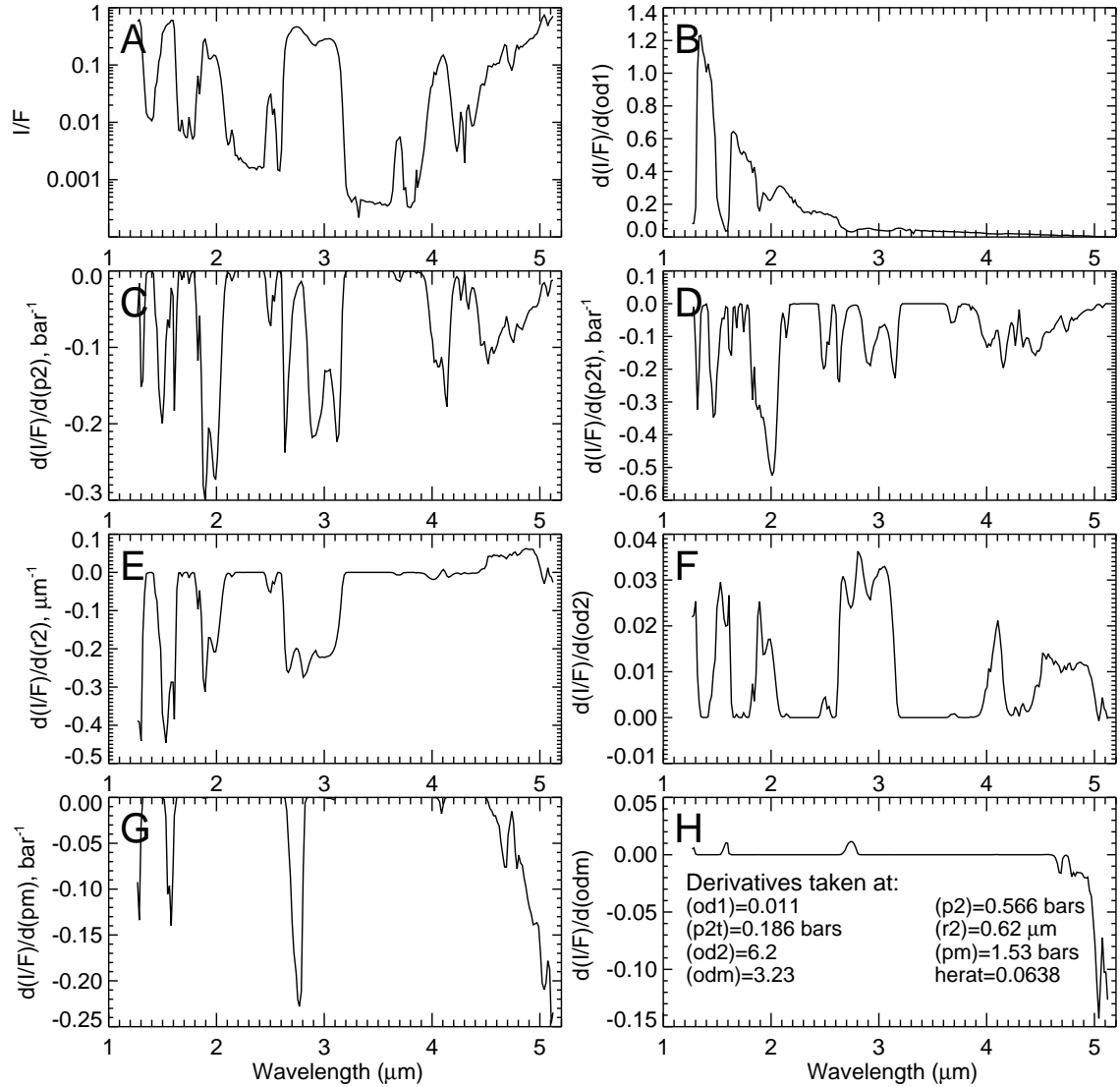


FIG. 7.— Model I/F spectrum (upper left) and spectral derivatives of I/F with respect to seven key model parameters described in the text. Panel H provides values of the parameters at which the derivatives were taken.

TABLE 2  
SUMMARY OF CLOUD MODEL PARAMETERS USED IN SPECTRAL CALCULATIONS.

$p1$ , bars	stratospheric haze pressure	0.002
$r1$ , $\mu\text{m}$	stratospheric haze particle radius	$0.14 \mu\text{m}$
$od1$	stratospheric haze optical depth	adjustable
$p2t$ , bars	top of upper cloud	adjustable
$p2$ , bars	bottom of upper cloud	adjustable
$r2$ , $\mu\text{m}$	radius of upper cloud particles	adjustable
$od2$	optical depth of upper cloud at $2 \mu\text{m}$	adjustable
$pm$ , bars	pressure of lower sheet cloud	adjustable
$odm$	optical depth of lower sheet cloud	adjustable
$\varpi$	single-scattering albedo of lower cloud	0.95
$g$	asymmetry parameter of lower cloud	0 (=isotropic)
$H_c/H_p$	cloud particle to gas scale height ratio	1.0

cloud properties ( $\varpi = 0.95$ ,  $g = 0$ ) do provide sufficient attenuation with a modest optical depth of 3.2. The pressure of this cloud is constrained by its role in shaping the thermal emission spectrum and in adding reflectivity in the continuum

TABLE 3  
CORRELATIONS BETWEEN FITTED PARAMETERS LISTED IN TABLE 2.

	$p2$	$p2t$	$r2$	$pm$	$od1$	$od2$	$odm$
$p2$	1.000	-0.915	0.096	0.505	-0.057	0.873	-0.317
$p2t$	-0.915	1.000	-0.207	-0.372	0.134	-0.706	0.227
$r2$	0.096	-0.207	1.000	0.129	0.068	0.259	0.011
$pm$	0.505	-0.372	0.129	1.000	-0.003	0.659	-0.719
$od1$	-0.057	0.134	0.068	-0.003	1.000	-0.015	0.008
$od2$	0.873	-0.706	0.259	0.659	-0.015	1.000	-0.389
$odm$	-0.317	0.227	0.011	-0.719	0.008	-0.389	1.000

regions at shorter wavelengths, especially near  $2.8 \mu\text{m}$  (see Fig. 7G).

Spectra from the 10 December 2012 observations (locations H and I in Fig. 9) are compared in Fig. 10, with the spectrum from the main wake region (H) shown as green and that from the AV core (I) shown as black. There is little difference between them in the thermal emission part of the spectrum ( $\lambda > 4.5 \mu\text{m}$ ). The more significant difference is at



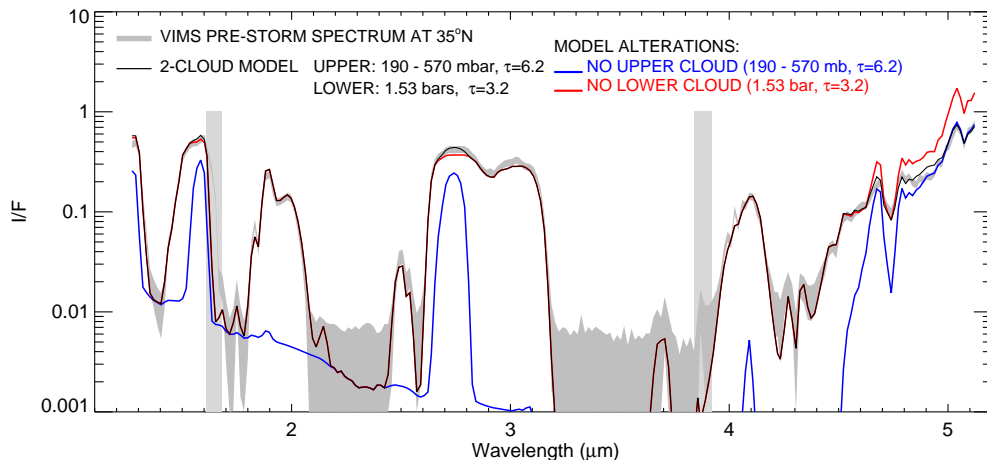


FIG. 8.— February 2011 VIMS spectrum upstream of the Great Storm (gray), model fit (black solid line), and spectra obtained by removing the upper cloud only (blue) and the lower cloud only (red). Because it consists of non-absorbing particles, the upper cloud does very little to attenuate the thermal emission. The measured spectrum was extracted from location A in Fig. 9. The vertical light gray bars indicate regions where the VIMS calibration is unusable due to effects of order-sorting filter joints.

continuum wavelengths that are controlled by scattered light from the upper cloud. Clearly the upper cloud is optically thinner over the anticyclone, although it still makes a significant contribution to the spectrum. Sample fits to the H spectrum, the region brightest at  $5 \mu\text{m}$  on 10 December 2012, are shown as black and green curves in Fig. 11 (other model spectra shown there are discussed in Sections 6.1 and 6.2). The corresponding cloud structures are displayed in Fig. 12. For  $\text{He}/\text{H}_2 = 0.064$ , and  $\text{PH}_3$  VMR = 4 ppm (with a uniform mixing ratio for  $p \geq 0.55$  bars and falling off with a gas/pressure scale height ratio of 0.5 for  $p < 0.55$  bars), the two-cloud model provides a better fit than the one-cloud model ( $\chi^2/N_F = 2.12$  vs. 2.39). The one-cloud model does not provide a high enough I/F near  $2.75 \mu\text{m}$ , which indicates the need for an additional cloud layer, but that cloud does not need to be an absorbing cloud and its inferred pressure (from the two-cloud model) is near 800 mb, rather than at the 1.5 – 1.6 bar level seen before and during the early stages of the clearing. Clearly, this cloud does not need to play a significant role in attenuating thermal emission.

Table 4 summarizes the main fit results from spectra containing both solar and thermal contributions, which we found provided better constraints on upper cloud structure than were possible with just night-side thermal emission spectra. The observing geometry for each spectrum we fit is given in Table 5. Note that these results are for  $\text{He}/\text{H}_2 = 0.064$ . The main parameters are plotted versus time in Fig. 13. Letter labels in this figure and the referenced tables refer to locations given in Fig. 9. The earliest observation we fit was obtained on 24 February 2011, from region A in that figure, immediately upstream of the Great Storm, before it was affected by the spreading wake. This represents the cloud structure before the “clearing-out” process in the wake took effect. The earliest observation we fit inside the wake was obtained on 11 May 2011 in the  $5\text{-}\mu\text{m}$  bright region in the vicinity of the large anticyclone (location B in Fig. 9), before it was overtaken by the Great Storm itself, which happened in June 2011. The anticyclone survived the encounter, and has remained through at least 19 August 2015 (Momary et al. 2015). By January 2012, the clearing process produced high emitted radiances that extended all the way around the planet, and by December 2012 it achieved a high degree of longitudinal uniformity, as well as a moderately high latitudinal uniformity within planetocentric

latitudinal boundaries from  $32^\circ$  N to  $39^\circ$  N (see Fig. 3).

### 5.3. Evolution of cloud structure in the “cleared” regions

Relative to the undisturbed cloud structure ahead of the storm, the earliest bright region we sampled (B) had 70% less upper-cloud optical depth and lower boundary pressures, as well as a factor of 4 – 5 less optical depth for the deeper cloud, with no difference in pressure. But as the wake clearing spread, the lower cloud in the cleared regions rose in altitude to near the 1-bar level. This might mean that the deeper lower cloud just disappeared and a previously insignificant layer became more noticeable. Most of the fits were made with a deep  $\text{PH}_3$  VMR of 4 ppm; with 5 ppm, the needed lower cloud opacities decrease somewhat, raising the possibility of a complete clearing of lower cloud particles. It is also conceivable that small reductions in temperature produce lower emissions, which in turn would require less blocking of those emissions and might also be consistent with a complete clearing of lower cloud particles. A 1 K change in effective temperature would produce about a 6% change in the emitted radiance at  $5 \mu\text{m}$ . The effect of the  $\text{He}/\text{H}_2$  ratio on the lower cloud properties, and how well spectra can be fit without a lower cloud, are discussed further in the following section.

### 5.4. Alternative models of cloud structure in the clearest regions

At middle latitudes, the  $5\text{-}\mu\text{m}$  brightest region on Saturn seems to be at the edge of the “cleared-out” band inside the core of what appears to be the remnant of the anticyclonic vortex (AV) that formed along with the Great Storm, but persisted for a much longer time interval (Sayanagi et al. 2013; Momary and Baines 2014; Momary et al. 2015). VIMS spectral observations from 10 December 2012, plotted in Fig. 10, show that this core region (H) is slightly brighter than the middle of the bright band (I), possibly because there is less high-altitude cloud optical depth to attenuate the thermal emission. At short wavelengths this core region is relatively darker than the middle of the band, which tends to support this speculation, although this effect should be small if the upper cloud is truly conservative. Spectral fits to the core region spectrum are shown in Fig. 14 for a range of  $\text{He}/\text{H}_2$  ratios. Even this region of very high  $5\text{-}\mu\text{m}$  brightness and low visible I/F is seen to have a significant optical depth of overlying cloud particles,

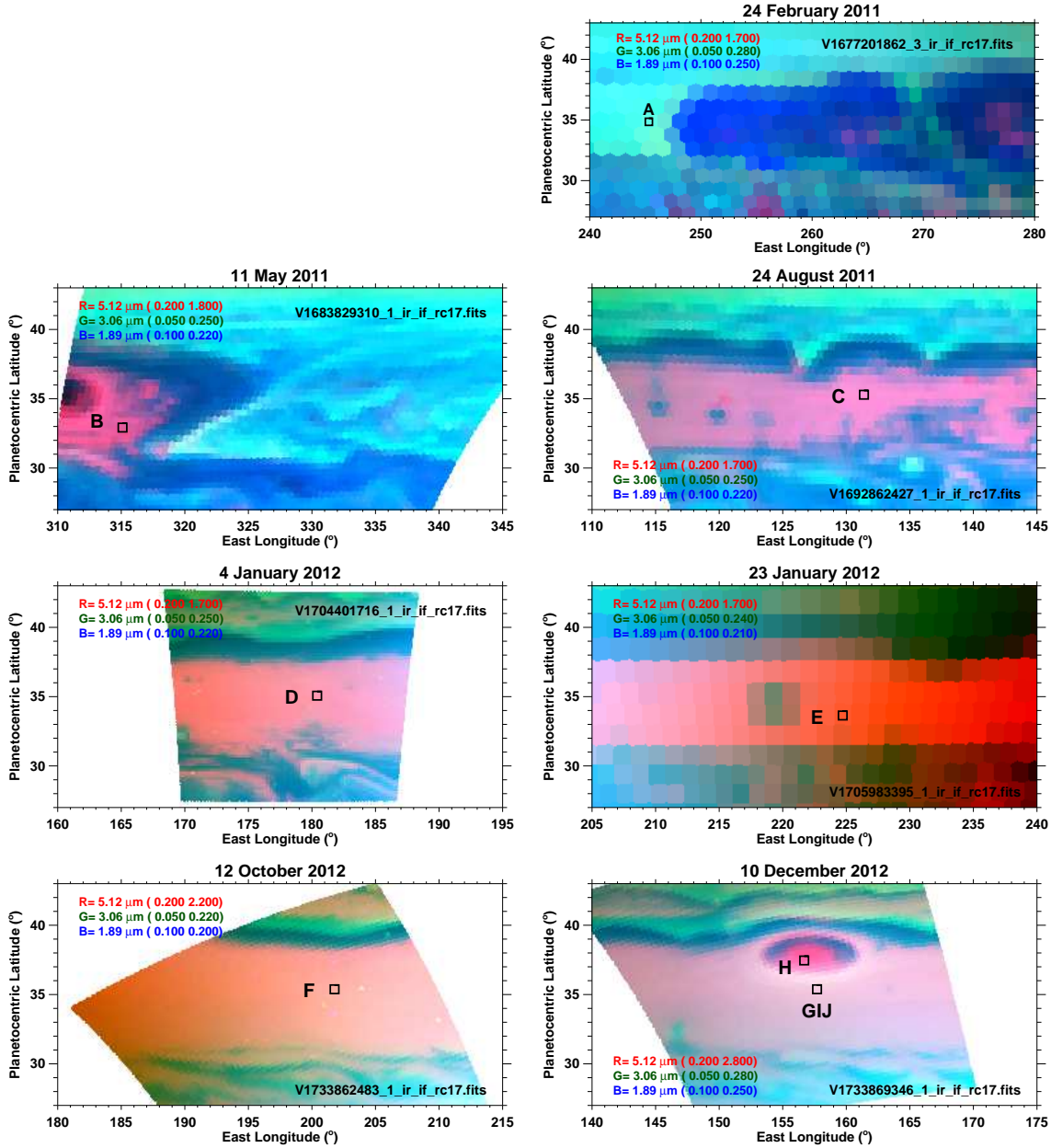


FIG. 9.— Color composite VIMS image of the Great Storm on 24 February 2011 (top) and selected images of the wake region on six dates from 11 May 2011 through 10 December 2012. R, G, and B channels are assigned to wavelengths of  $5.12 \mu\text{m}$ ,  $3.06 \mu\text{m}$ , and  $1.89 \mu\text{m}$ , with stretches given in the legends. In each image the location(s) of spectral samples are marked by black squares and labeled A–J, for which fit results are presented in Table 4. In May 2011 and December 2012 images, the oval feature is the anticyclonic vortex labeled as AV in Fig. 3, which also provides a larger context for all but the October sample.

increasing from  $\sim 3.5$  to  $\sim 5.5$  for  $\text{He}/\text{H}_2$  ratios from 0.02 to 0.09.

#### 5.4.1. Fits of two-cloud models as a function of the $\text{He}/\text{H}_2$ ratio

When we model the structure using two clouds, we find that the upper cloud layer extends from 150 mbar to 250 mbar and has an optical depth near 4, with little dependence on the assumed  $\text{He}/\text{H}_2$  ratio. Fit quality is also maintained over a wide range of  $\text{He}/\text{H}_2$  ratios, mainly by adjusting the  $\text{PH}_3$  mixing ratio and the lower cloud optical depth and pressure. The inferred properties of the lower cloud in our model vary significantly with the assumed  $\text{He}/\text{H}_2$  ratio. At large values of that ratio, the sheet cloud is found near 1.8 bars, with an optical depth of 1.6 to 2.4 for deep  $\text{PH}_3$  mixing ratios from  $6 \times 10^{-6}$  to  $4 \times 10^{-6}$ , respectively. As the  $\text{He}/\text{H}_2$  ratio decreases the

optical depth of the lower cloud also decreases, reaching zero at a  $\text{He}/\text{H}_2$  ratio of 0.05 for a  $\text{PH}_3$  VMR of  $4 \times 10^{-6}$ , at a  $\text{He}/\text{H}_2$  ratio of  $0.064 \times 10^{-6}$  for a  $\text{PH}_3$  VMR of  $5 \times 10^{-6}$ , and at larger ratios for larger values of the  $\text{PH}_3$  mixing ratio. Even though we found a non-zero optical depth for the lower cloud at  $\text{He}/\text{H}_2 = 0.064$ , that cloud is not providing any significant attenuation of the thermal emission at that point. In fact, if we make this lower cloud conservative (setting  $\varpi = 1.0$ ), as for fit H in Table 4, the results is a better fit and an even smaller optical depth. Thus, at this value of the  $\text{He}/\text{H}_2$  ratio, there is really no evidence for a deep absorbing cloud, although one is clearly required at larger  $\text{He}/\text{H}_2$  ratios (assuming fixed trace gas profiles). We next consider an even simpler cloud structure without a deep absorbing cloud.

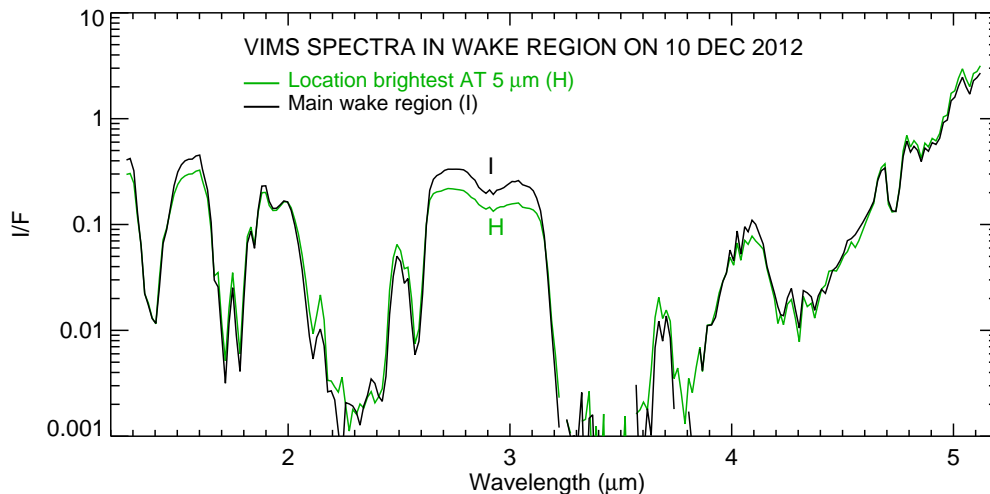


FIG. 10.— Comparison of 10 December 2012 spectra obtained in the central wake region (location I in Fig. 9) and the 5- $\mu\text{m}$  brightest region in the center of the anticyclonic vortex (location H). Note that the latter is darker at continuum wavelengths below 4.5  $\mu\text{m}$  where reflected sunlight dominates, indicating reduced upper cloud optical depth.

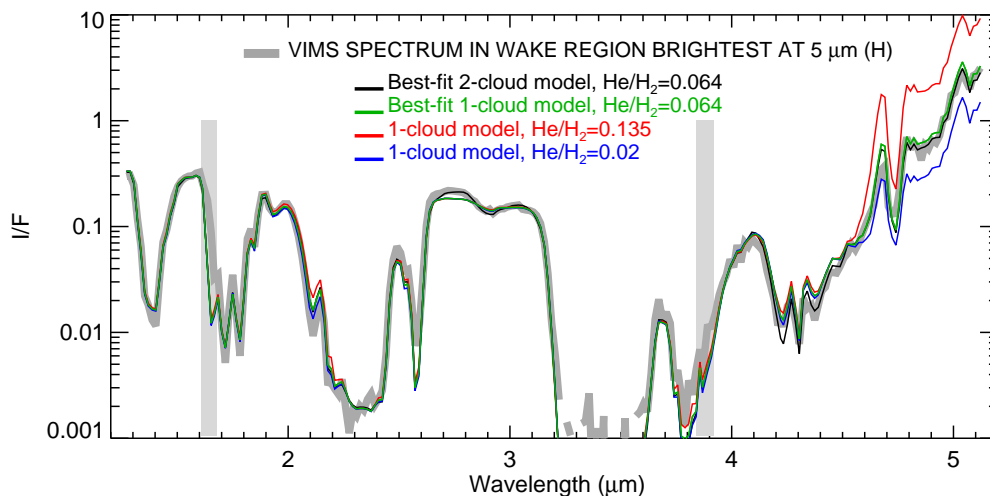


FIG. 11.— A spectrum measured in the core of the anticyclone (gray thick line) and alternative fits using a two-cloud model (thin black line) and a one-cloud model (green line). Also shown are spectra computed from the one-cloud model parameters, but with temperature profiles for  $\text{He}/\text{H}_2 = 0.02$  (blue) and  $\text{He}/\text{H}_2 = 0.135$  (red). These are discussed in Sections 6.1 and 6.2. The vertical light gray bars indicate regions where the VIMS calibration is unusable due to effects of order-sorting filter joints.

#### 5.4.2. Fits of one-cloud models as a function of the $\text{He}/\text{H}_2$ ratio

Next we consider solutions for which the deep sheet cloud is entirely absent, solutions for which there are no aerosols present between the upper cloud and the 5-bar region, the approximate location of the peak in the thermal emission contribution function. These fits are shown in Fig. 14E-H. In this case, the optical depth of the upper cloud does vary with the  $\text{He}/\text{H}_2$  ratio, as does its particle size. The  $\chi^2$  plot (H) shows that there is also a strong preference for a  $\text{He}/\text{H}_2$  ratio  $\approx 0.064$  and a  $\text{PH}_3$  VMR  $\approx 5 \times 10^{-6}$ . With  $\text{He}/\text{H}_2$  ratios 0.03 greater or 0.03 smaller than this value fit quality becomes dramatically worse no matter what value of the  $\text{PH}_3$  mixing ratio is chosen. However, this result is somewhat misleading because it is a consequence of how we adjusted the  $\text{PH}_3$  mixing ratio profile. By varying the entire profile by the same fraction as the deep mixing ratio we actually made it difficult to fit the  $\text{PH}_3$  absorption feature between 4.1 and 4.5  $\mu\text{m}$ , which is a feature in reflected sunlight that is not much affected by changing the  $\text{He}/\text{H}_2$  ratio, as evident from the lack of variation shown in

Fig. 11. Thus there is no benefit to varying the  $\text{PH}_3$  profile at low pressures (100 – 500 mbar) when changes need to be made at higher pressures to control thermal emission. In the following section we discuss a different style of  $\text{PH}_3$  profile adjustment, in which only deeper mixing ratios are varied.

## 6. USING THE ONE-CLOUD MODEL TO CONSTRAIN ABSORBING GAS MIXING RATIOS

If we are to explain the great longitudinal uniformity and high 5- $\mu\text{m}$  brightness that developed in the wake of the Great Storm as a dynamical clearing of cloud particles below the upper cloud, then the single-cloud model fits tell us under what conditions that explanation is possible. For our previously assumed style of  $\text{PH}_3$  variation, and without varying any other trace gases, the best matches to VIMS spectra appeared to occur with a  $\text{He}/\text{H}_2$  ratio  $\approx 0.064 \pm 0.02$ . However, the range of acceptable  $\text{He}/\text{H}_2$  ratios can be expanded considerably if we adjust just the deep  $\text{PH}_3$  profile and also allow arbitrary adjustment of the arsine and ammonia mixing ratios. The following two extreme cases provide instructive examples.

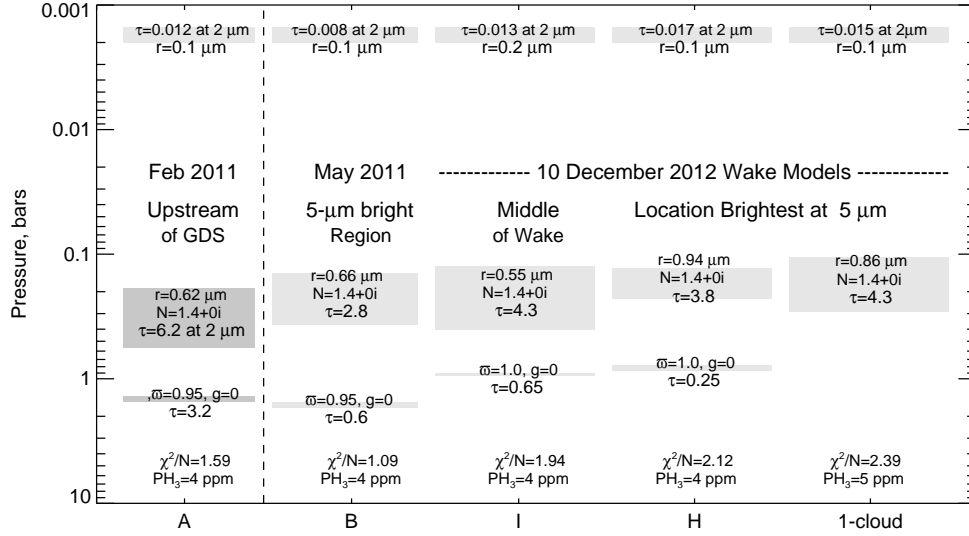


FIG. 12.— Comparison of the two-cloud model (A) for the region upstream of the Great Storm with two-cloud models (B, I, and H) for selected 5- $\mu\text{m}$  bright wake regions, and with the best-fit one-cloud model from Fig. 14, which is discussed in Sec. 5.4. The above letter labels correspond to those given in Table 4 and Fig. 9.

TABLE 4  
FIT RESULTS FOR 5- $\mu\text{m}$  BRIGHT REGIONS IN THE WAKE OF SATURN'S GREAT STORM OF 2010-2011.

ID	$p2t$ (mbar)	$p2$ (mbar)	$r2$ ( $\mu\text{m}$ )	$od2$	$pm$ (bar)	$odm$	$\chi^2$	PC Lat.	East Lon.	MM/DD/YYYY
A	$189^{+16}_{-46}$	$566^{+113}_{-103}$	$0.62^{+0.05}_{-0.05}$	$6.20^{+0.95}_{-0.88}$	$1.53^{+0.23}_{-0.16}$	$3.23^{+0.47}_{-0.53}$	54.0	$34.9^\circ$	$245.3^\circ$	02/24/2011
B	$141^{+25}_{-32}$	$367^{+44}_{-34}$	$0.66^{+0.06}_{-0.05}$	$2.83^{+0.20}_{-0.18}$	$1.72^{+0.11}_{-0.09}$	$1.07^{+0.10}_{-0.10}$	28.6	$32.9^\circ$	$315.1^\circ$	05/11/2011
C	$141^{+24}_{-30}$	$390^{+57}_{-45}$	$0.58^{+0.04}_{-0.03}$	$3.42^{+0.25}_{-0.23}$	$1.57^{+0.19}_{-0.13}$	$0.77^{+0.11}_{-0.10}$	37.9	$35.3^\circ$	$131.4^\circ$	08/24/2011
D	$157^{+29}_{-46}$	$366^{+97}_{-64}$	$0.57^{+0.05}_{-0.05}$	$3.81^{+0.36}_{-0.34}$	$1.33^{+0.26}_{-0.12}$	$0.71^{+0.11}_{-0.10}$	41.9	$35.1^\circ$	$180.4^\circ$	01/04/2012
E	$150^{+13}_{-15}$	$360^{+0}_{-0}$	$0.50^{+0.04}_{-0.03}$	$3.30^{+0.32}_{-0.30}$	$1.00^{+0.15}_{-0.11}$	$0.88^{+0.08}_{-0.07}$	29.1	$33.6^\circ$	$224.7^\circ$	01/23/2012
F	$138^{+30}_{-38}$	$344^{+86}_{-60}$	$0.55^{+0.04}_{-0.04}$	$3.67^{+0.72}_{-0.62}$	$0.82^{+0.24}_{-0.08}$	$0.58^{+0.10}_{-0.09}$	39.8	$35.4^\circ$	$201.8^\circ$	10/12/2012
G	$120^{+29}_{-30}$	$438^{+100}_{-82}$	$0.57^{+0.05}_{-0.05}$	$4.80^{+0.90}_{-0.82}$	$1.04^{+0.29}_{-0.19}$	$0.57^{+0.14}_{-0.12}$	66.4	$35.2^\circ$	$157.7^\circ$	12/10/2012
H	$128^{+41}_{-51}$	$227^{+96}_{-26}$	$0.94^{+0.13}_{-0.12}$	$3.79^{+0.53}_{-0.49}$	$0.86^{+0.44}_{-0.14}$	$0.25^{+0.12}_{-0.09}$	63.6	$37.5^\circ$	$156.7^\circ$	12/10/2012
I	$125^{+29}_{-32}$	$403^{+84}_{-76}$	$0.55^{+0.08}_{-0.07}$	$4.29^{+0.82}_{-0.74}$	$0.95^{+0.20}_{-0.12}$	$0.65^{+0.14}_{-0.12}$	63.7	$35.2^\circ$	$157.7^\circ$	12/10/2012
J	$104^{+28}_{-28}$	$455^{+89}_{-90}$	$0.56^{+0.06}_{-0.06}$	$4.65^{+1.27}_{-1.11}$	$0.74^{+1.63}_{-0.06}$	$0.40^{+0.19}_{-0.14}$	77.4	$35.2^\circ$	$157.7^\circ$	12/10/2012

Note: the first fit (A) is for a region upstream of the Great Storm and undisturbed by the wake. The remaining fits are for regions inside the wake that exhibit high 5- $\mu\text{m}$  emission. The deep phosphine VMR was set to 4 ppm for fits above the double line (A-I) and the profile was scaled to produce a deep VMR of 5 ppm for fit J. Fits H and I used  $\varpi = 1$  for the lower cloud, while the rest used  $\varpi = 0.95$ . Fit H is for the brightest 5- $\mu\text{m}$  region. Observing geometry is given in Table 5, and the locations from which fitted spectra were extracted are identified in Fig. 9.

TABLE 5  
OBSERVING GEOMETRY FOR SPECTRAL FITS IN TABLE 4.

ID	Observer zenith angle	Solar zenith angle	Azimuth angle	Phase angle
A	$51.31^\circ$	$28.98^\circ$	$98.52^\circ$	$51.81^\circ$
B	$39.13^\circ$	$24.00^\circ$	$139.64^\circ$	$23.14^\circ$
C	$40.66^\circ$	$34.16^\circ$	$154.67^\circ$	$15.37^\circ$
D	$40.59^\circ$	$53.21^\circ$	$98.19^\circ$	$56.04^\circ$
E	$35.82^\circ$	$68.82^\circ$	$87.66^\circ$	$74.10^\circ$
F	$27.81^\circ$	$55.41^\circ$	$146.17^\circ$	$36.41^\circ$
G	$16.37^\circ$	$39.72^\circ$	$132.68^\circ$	$31.25^\circ$
H	$15.75^\circ$	$40.84^\circ$	$138.91^\circ$	$31.25^\circ$
I	$16.37^\circ$	$39.72^\circ$	$132.68^\circ$	$31.25^\circ$
J	$16.37^\circ$	$39.72^\circ$	$132.68^\circ$	$31.25^\circ$

### 6.1. Adjusting gas profiles to improve fits with $\text{He}/\text{H}_2 = 0.02$ .

The one-cloud model from Fig. 12 was optimized for  $\text{He}/\text{H}_2 = 0.064$  and the nominal trace gas profiles. If we use that cloud model to compute a spectrum for the thermal structure appropriate to a  $\text{He}/\text{H}_2$  ratio of 0.02, we see from blue curve in Fig. 11 that the resulting spectrum remains a good fit in reflected sunlight, but falls a dramatic factor of two short of the observed I/F in the thermal emission region. This discrepancy is shown in greater detail in Fig. 15, where the blue curve is for the same model shown by that color in Fig. 11. The other curves in Fig. 15 show how that discrepancy can be fixed, first by drastically reducing the  $\text{NH}_3$  mixing ratio (producing the red curve), then by also reducing just the deep  $\text{PH}_3$  mixing ratio (producing the green curve) and finally by dropping the arsine volume mixing ratio to 3 ppb (producing the black curve). Because  $\text{NH}_3$  is the dominant absorber for  $\lambda > 5.1 \mu\text{m}$  (see Fig. 4), the  $\text{NH}_3$  mixing ratio had to be

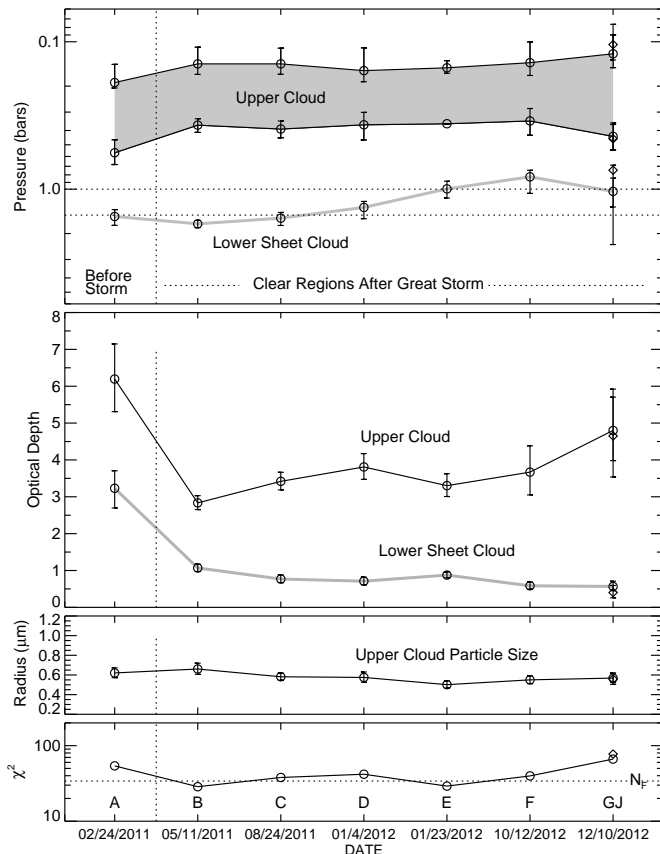


FIG. 13.— Main fit parameters for vertical cloud structure models constrained by reflected solar and thermal spectra from “clear” ( $5\text{-}\mu\text{m}$  bright) regions, as a function of time. The initially low upper cloud opacity seems to be slowly returning to the optical depth it had prior to the Great Storm, although the larger uncertainty in the later points leaves open the possibility that the trend is not real. The letter labels in the bottom panel refer to fits in Table 4 and locations in Fig. 9. Points plotted with diamond symbols are for fit J, for which the  $\text{PH}_3$  profile was scaled to make the deep mixing ratio equal 5 ppm. This slightly reduces the best-fit optical depth of the lower cloud and moves it to lower pressures, towards the bottom of the upper cloud. The worsening fit quality at later times may be due to drifts in the VIMS spectral scale.

reduced to negligible levels to boost emission in that region. These modifications result in a  $\chi^2/N_f$  of 3.09, evaluated for the 38 spectral points beyond  $4.5\ \mu\text{m}$ . The corresponding value for the  $\text{He}/\text{H}_2 = 0.064$  spectrum is a significantly worse 4.55, even after some fine tuning of the scale height ratio.

Note that our above adjustment of the  $\text{PH}_3$  profile was designed to affect the thermal emission without affecting the reflected solar model by keeping the mixing ratio the same at lower pressures and preserving the falloff rate down to the level at which it intersects the chosen deep mixing ratio. To change the deep mixing ratio from  $\alpha_0$  to  $\alpha_x$  without changing the VMR profile above the original break-point, we pick a new pressure break-point  $P_x = P_0(\alpha_x/\alpha_0)^{f/(1-f)}$ , where  $f$  is the original scale height ratio. The profile we selected to optimize the model spectrum for  $\text{He}/\text{H}_2 = 0.02$  is shown by the black dot-dash profile in Fig. 16, where the nominal profile (for  $\text{He}/\text{H}_2 = 0.064$ ) is shown as a solid black line.

### 6.2. Adjusting gas profiles to improve fits with $\text{He}/\text{H}_2 = 0.135$ .

In this case, using the nominal one-cloud model to compute a spectrum for a thermal structure appropriate to  $\text{He}/\text{H}_2 = 0.135$ , we see from the red curve in Fig. 11 that although

the reflected sunlight dominated part of the spectrum remains well fit, the model spectrum exceeds observations by more than a factor of three in the thermal emission region. A more detailed view of this region is displayed in Fig. 17, where the red curve is for the same model represented by that color in Fig. 11. This figure also shows how the large discrepancy can be greatly reduced by increasing the deep  $\text{PH}_3$  VMR from 4 ppm to 8 ppm and increasing the pressure break point from 550 mbar to 1.1 bars (producing the blue curve), by also increasing the deep  $\text{NH}_3$  mixing ratio to  $6 \times 10^{-4}$  (producing the green curve), and finally, by doubling the arsine VMR to 12 ppb (producing the black curve). The  $\text{PH}_3$  profile we used here is displayed by the black dotted curve in Fig. 16. The adjusted ammonia profile is shown by the dot-dash curve in Fig. 18, where the nominal Prinn et al. (1984) profile is shown by the dashed curve. The final model spectrum is a poorer fit than we were able to achieve for low values of  $\text{He}/\text{H}_2$ , and required an amount of  $\text{NH}_3$  that we will show exceeds other independent estimates in the critical 1 – 4 bar region. Thus, this solution seems less plausible.

### 6.3. Direct spectral comparison of fits at different $\text{He}/\text{H}_2$ ratios.

Cloud structure and gas mixing ratio models were optimized to match the thermal emission spectra without disturbing fit quality in the reflected solar dominated part of the spectrum. However, these actually did lead to small differences near  $2.1\ \mu\text{m}$  as a result of different degrees of hydrogen absorption that are visible in this methane window region (see Fig. 4). Fig. 19 compares fits for three different  $\text{He}/\text{H}_2$  ratios both in the  $1.8\text{-}2.3\ \mu\text{m}$  region (left panel) and in the thermal emission dominated region (right panel). Both comparisons seem to favor the lower  $\text{He}/\text{H}_2$  ratios in overall fit quality. However, some of the small scale features in the measurements in the  $4.8\text{-}5.15\ \mu\text{m}$  region are smoothed over too much by the  $\text{He}/\text{H}_2 = 0.02$  fit, and better matched by  $\text{He}/\text{H}_2 = 0.064$  fit.

We found no models that were able to provide a good fit at both  $4.67\ \mu\text{m}$  and  $4.74\ \mu\text{m}$ . Most models produce spectra that were too high at the former and too low at the latter, and this wavelength region contributed a substantial fraction of the  $\chi^2$  for the thermal fits (lower right panel of Fig. 19). Nor was any model able to reproduce the small dip near  $4.85\ \mu\text{m}$ . Fletcher et al. (2011) also noted similar problems at  $4.67\ \mu\text{m}$  and  $4.85\ \mu\text{m}$ , as well as an under-fitting problem at  $5.06\ \mu\text{m}$ , which did not stand out in our modeling. At shorter wavelengths we also noted problems in fitting the  $4.3\text{-}\mu\text{m}$   $\text{PH}_3$  band, for which models tended to be more asymmetric than the observations, as can be seen in Fig. 11. We also were unable to closely reproduce the depth of the methane absorption feature at  $2.58\text{-}\mu\text{m}$ , also visible in Fig. 11. Whether any of these problems might be resolved by improved line data remains to be determined.

### 7. USING INDEPENDENT GAS CONSTRAINTS TO CONSTRAIN $\text{He}/\text{H}_2$ RATIOS.

We have shown that the lack of a deep absorbing cloud in the putative clear regions increases thermal emission at high  $\text{He}/\text{H}_2$  ratios and decreases thermal emission at low  $\text{He}/\text{H}_2$  ratios. We have also shown that these changes can be largely compensated for by adjusting the vertical profiles of  $\text{PH}_3$  and  $\text{AsH}_3$ . Here we consider other constraints on these gas profiles that might be inconsistent with such adjustments, and thus provide limits on the range of acceptable  $\text{He}/\text{H}_2$  ratios.

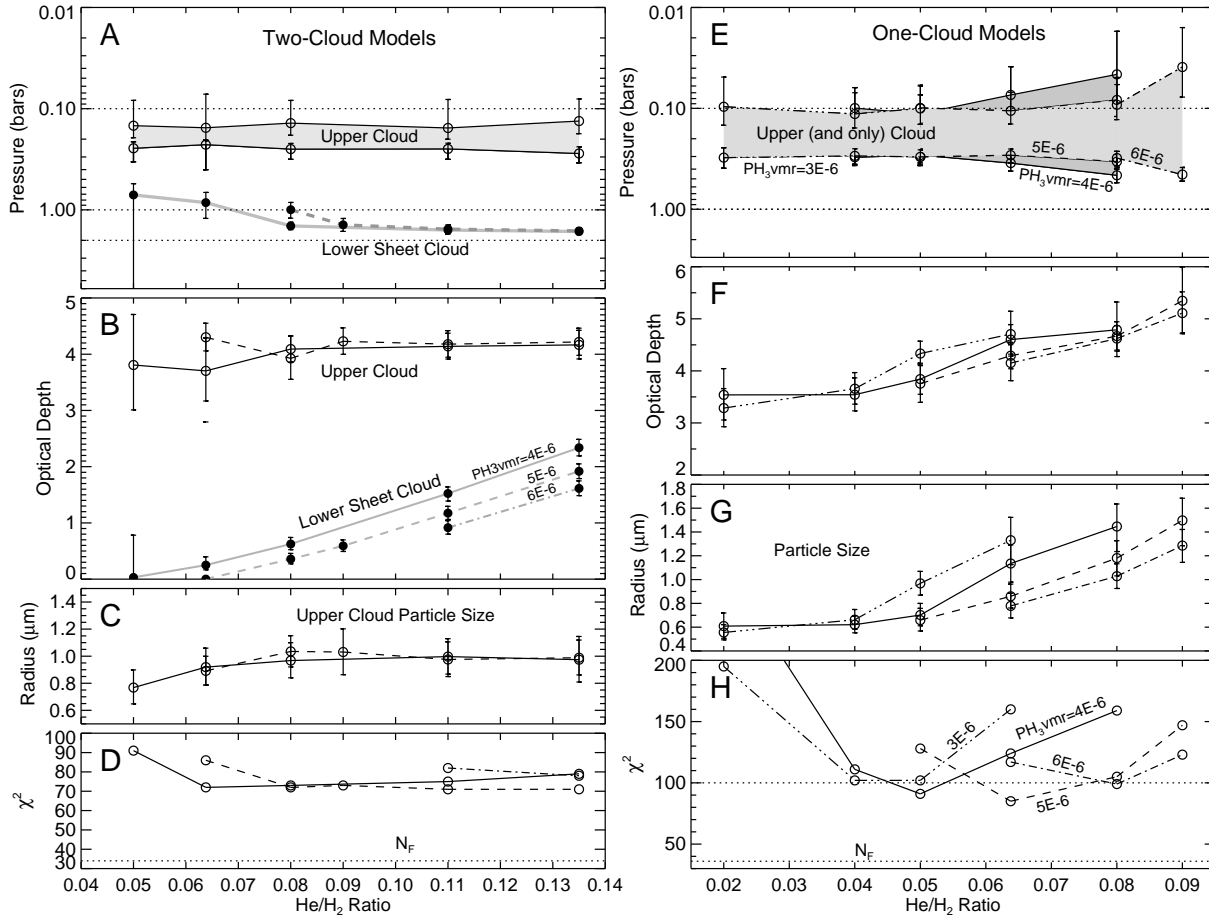


FIG. 14.— Cloud structure inferred from one of the clearest regions on Saturn as a function of the assumed He/H<sub>2</sub> ratio for two-cloud models (A-D, left) and one-cloud models (E-H, right). Note that the  $\chi^2$  values for the two-cloud model are nearly flat vs. He/H<sub>2</sub> ratio and reach a lower minimum (70) than the one-cloud model (86). The reduced  $\chi^2$  values ( $\chi^2/N_F$ ) are 2.09 and 2.39 respectively.

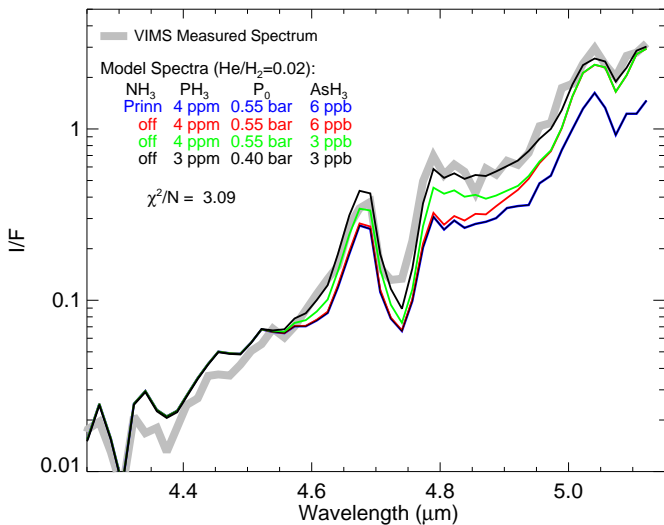


FIG. 15.— Modifications of absorbing gas mixing ratio profiles to obtain optimum fits in the brightest wake region assuming a He/H<sub>2</sub> ratio of 0.02 and no deep absorbing cloud. In this case greatly reduced absorption is needed to boost the model I/F to the observed level (gray curve). The best-fit vertical mixing ratio profile for PH<sub>3</sub> is shown as a dotted line in Fig. 16. The NH<sub>3</sub> profile for this case must be much less than the standard profile, but not constrained to a specific value. All the model profiles for PH<sub>3</sub> use  $f = 0.5$ .

## 7.1. Limits to phosphine adjustments

### 7.1.1. CIRS-VIMS comparisons

In Fig. 16A, the PH<sub>3</sub> profiles we derived for the clearest region of the wake are compared with CIRS results of Fletcher et al. (2009a) and night-side VIMS results of Fletcher et al. (2011). As indicated by gray bars in the figure (panel B), CIRS results are sensitive to PH<sub>3</sub> in the 400 – 800 mbar range, while VIMS night-side spectra are sensitive to PH<sub>3</sub> in the 1.2 – 7 bar range (roughly), according to Fig. 6 of Fletcher et al. (2011). While CIRS results include a substantial latitudinal variation, here we show only example results from 35° N and 35° S (planetocentric). The night-side VIMS results of Fletcher et al. (2011) are shown only for 35° N and for two different retrieval models, one with a non-scattering gray absorbing cloud and a second that includes a scattering cloud. Both models have smaller deep VMR values and smaller scale heights than other results.

Although these Fletcher et al. (2011) night-side retrievals of PH<sub>3</sub> show considerable variability depending on what type of cloud model is assumed, the large discrepancy between the night-side results and the CIRS results in the 400 – 800 mb range is a robust characteristic. This is surprising, especially given that our inferred PH<sub>3</sub> profile is in much better agreement with CIRS results in the range where CIRS is sensitive to PH<sub>3</sub>. Most of these profiles are characterized by a constant mixing ratio for  $P > P_b$  and a decline with altitude with

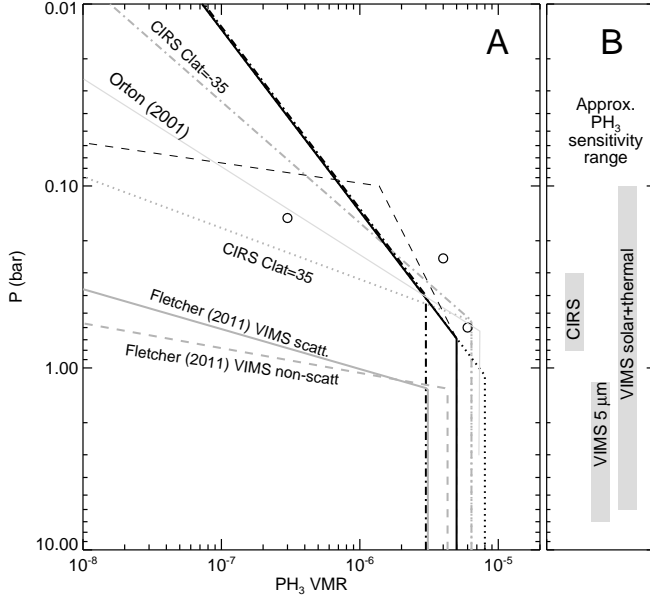


FIG. 16.— A: Phosphine profiles we inferred from fitting the brightest “cleared” region of the wake assuming no deep absorbing cloud, are shown as dark lines, using solid for  $\text{He}/\text{H}_2 = 0.064$ , dot-dash for  $\text{He}/\text{H}_2 = 0.02$ , dotted for  $\text{He}/\text{H}_2 = 0.135$ , and dashed for the three-slope profile yielding the same fit quality as the solid profile, but is more compatible with the sharper cutoff of the Lellouch et al. (2001) results (open circles). For comparison phosphine profiles from CIRS (Fletcher et al. 2009a) and VIMS (Fletcher et al. 2011) are also shown using lighter lines. The Orton et al. (2001) result (lightest gray line) is based on sub-mm groundbased observations and represents a disk average. The CIRS and Fletcher et al. (2011) results are based entirely on thermal emission spectra and assume a  $\text{He}/\text{H}_2$  ratio of 0.135. B: Sensitivity ranges (to  $\text{PH}_3$ ) for the CIRS and VIMS 5- $\mu\text{m}$  spectra are according to Fig. 6 of Fletcher et al. (2011). The sensitivity range indicated for VIMS solar+thermal spectra is bounded by twice the unit optical depth range from our Fig. 4 for regions of the spectrum where phosphine is dominant, e.g. near 2.8 – 3  $\mu\text{m}$  and 4.1 – 5.1  $\mu\text{m}$ . Note the order of magnitude disagreement between the CIRS and Fletcher et al. (2011) VIMS results in the 800 mb region. In the same region our VIMS results are relatively consistent with CIRS results, considering the substantial variability that has been observed.

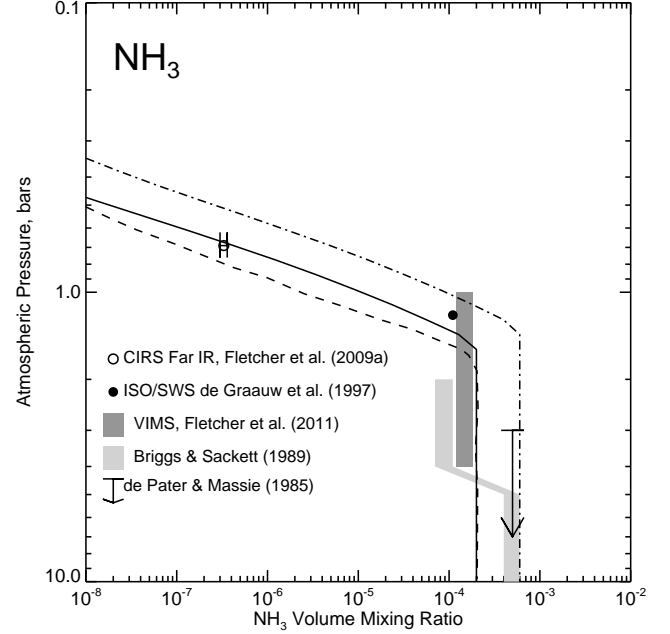


FIG. 18.— Ammonia profiles we used to adjust emitted radiation to be consistent with the brightest clear wake spectrum are indicated by dashed (for  $\text{He}/\text{H}_2 = 0.064$ ) and dot-dash (for  $\text{He}/\text{H}_2 = 0.135$ ). The dashed curve is from Prinn et al. (1984) and the solid curve shows the saturated vapor profile with the same deep mixing ratio. For  $\text{He}/\text{H}_2 = 0.02$  no profile is plotted because we assumed ammonia was depleted by more than an order of magnitude, and thus negligible. Independent observations are identified in the legend and discussed in the text.

a scale height that has a constant ratio to the pressure scale height, following Eq. 1. The exception is the three slope profile shown by the black dashed curve in Fig. 16. In that case there are two pressure break points  $P_0$  and  $P_1$  and two scale heights  $f$  and  $f_1$ , and the upper region of the profile satisfies Eq. 2, while Eq. 1 applies for  $P_0 > P > P_1$ .

### 7.1.2. Constraints from the 4.1 – 4.6 $\mu\text{m}$ band

The large discrepancy between CIRS and VIMS  $\text{PH}_3$  profiles is especially easy to detect in the reflected solar spectrum, as illustrated in Fig. 20. Here we see large differences in spectral shape in the 4.1 – 4.5  $\mu\text{m}$  region, with the best match to observed spectra occurring with our nominal profile and the CIRS B profile (which has a larger scale height fraction derived from 35°S). The 4.1 – 4.6  $\mu\text{m}$  wavelength range is where reflected sunlight is especially sensitive to the  $\text{PH}_3$  mixing ratio in the 100 – 500 mbar pressure range. The night-side VIMS profile of Fletcher et al. (2011) produces essentially no detectable absorption feature in this spectral region. It also produces excessive I/F values at thermal emission wavelengths because of its relatively low deep VMR (for its assumed  $\text{He}/\text{H}_2$  ratio of 0.135). The spectral matches to the much smaller absorption feature near 2.9  $\mu\text{m}$  are consistent with what is seen at longer reflected solar wavelengths. These results make a strong case for using both solar and thermal spectral regions in combination to constrain the vertical profile of phosphine. The 4.1 – 4.5  $\mu\text{m}$  absorption band is evidently an important one for constraining  $\text{PH}_3$  on Saturn, but has seen little use so far.

### 7.1.3. Constraints from ISO and groundbased observations

Disk-averaged values have been derived by a number of observers based on high spectral resolution observations that can

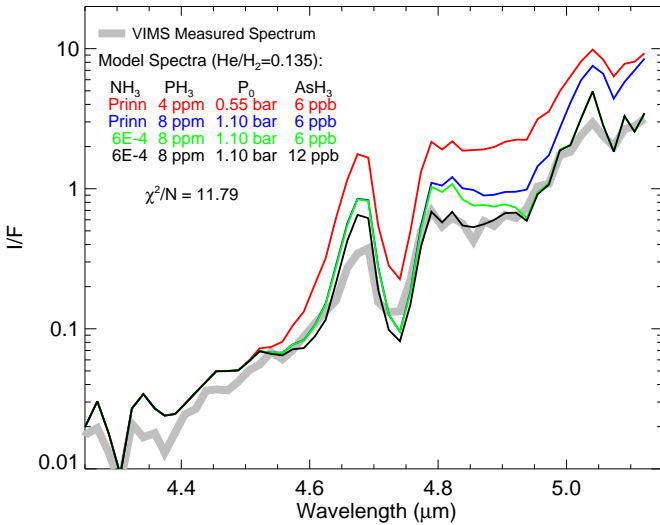


FIG. 17.— Modifications of absorbing gas mixing ratio profiles to obtain optimum fits in the brightest wake region assuming a  $\text{He}/\text{H}_2$  ratio of 0.135 and no deep absorbing cloud. In this case greatly increased absorption is needed to reduce the model I/F to the observed level (gray curve). The best-fit vertical mixing ratio profiles for this case are shown as dot-dash lines in Fig. 16 for  $\text{PH}_3$  and in Fig. 18 for  $\text{NH}_3$ . All model profiles for  $\text{PH}_3$  use  $f = 0.5$ .

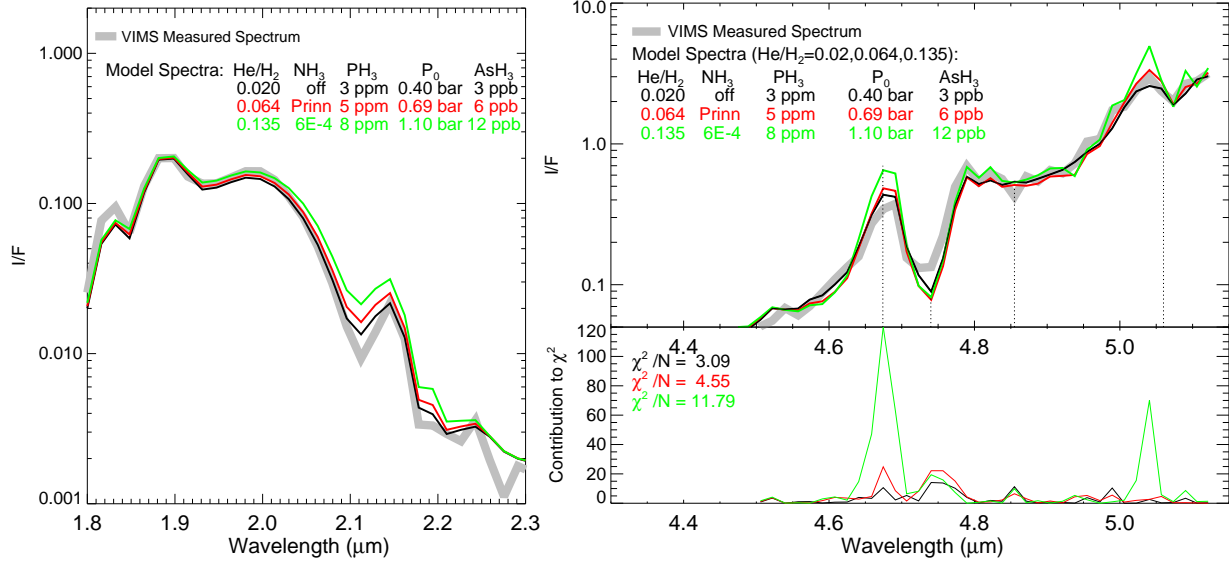


FIG. 19.— Comparison of one-cloud best-fit models of the brightest wake thermal emission spectrum for three different He/H<sub>2</sub> ratios, at both solar-dominated wavelengths (left panel) and thermal-dominated wavelengths (right panel). The vertical mixing ratio profiles for PH<sub>3</sub> and NH<sub>3</sub> for these models are shown in Figs. 16 and 18 respectively. All models use  $f = 0.5$ . Vertical dotted lines are plotted in the right panel to identify regions of spectral fitting problems discussed in the text.

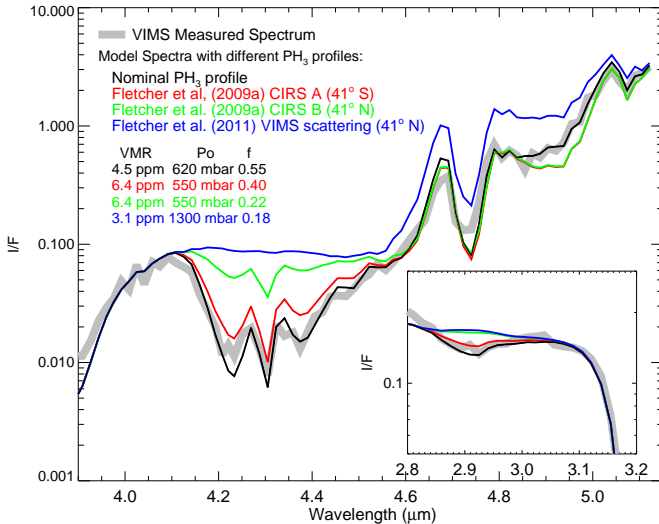


FIG. 20.— Model spectra for different PH<sub>3</sub> profiles shown in Fig. 16. All profiles assume a uniform deep VMR for  $P \geq P_0$  and an exponential decline for  $P \leq P_0$  with a PH<sub>3</sub> to pressure scale height ratio of  $f$ , with specific parameter values shown in the inset table. Except for the Fletcher et al. (2011) VIMS-based profile, all the PH<sub>3</sub> profiles yield similar thermal emission spectra. But very large differences are seen at reflected solar wavelengths, which are sensitive to PH<sub>3</sub> mixing ratios at lower pressures as well as higher pressures (inset). Note that the observed 4.3-μm PH<sub>3</sub> band is measured to be more symmetric about 4.3 μm than our models indicate.

resolve more distinctive spectral features of PH<sub>3</sub> in the thermal emission range of Saturn’s spectrum and are thus probably less sensitive to different assumptions of He/H<sub>2</sub> ratios and less sensitive to assumed cloud properties. Lellouch et al. (2001) used ISO/SWS observations of the 8.1 – 11.3 μm spectrum to infer PH<sub>3</sub> mixing ratios in the 100 – 600 mbar range, with a value of 6 ppm up to 600 mbar, 4 ppm at 250 mb, decreasing to 0.3 ppm at 150 mbar. These are plotted as open circles in Fig. 16. Also shown there using a gray solid line is the profile inferred by Orton et al. (2001) from sub-mm thermal emission observations. The falloff of PH<sub>3</sub> VMR with altitude is an expected result of photochemical destruction. Although

the falloff rate is not well defined, it is probably sharper than most of these profiles indicate.

Fig. 21 displays deep PH<sub>3</sub> VMR values as a function of the He/H<sub>2</sub> ratio assumed in our analysis of the VIMS emission spectrum from the brightest region of the wake. Also shown are independent determinations of the ratio from high-resolution 5-μm spectra by Noll et al. (1990), from ISO-SWS spectra by Lellouch et al. (2001), and from sub-mm spectra by Orton et al. (2000, 2001). Orton et al. (2000) note that a 25% reduction in PH<sub>3</sub> (i.e. from 7.4 ppm to 5.6 ppm) would be produced by a 2° decrease in the assumed temperature at all pressures, which they noted would provide a slightly better fit for the 3-2 line. It would also provide better agreement with Lellouch et al. (2001) and Fletcher et al. (2009a). No specific error estimates were provided for the Lellouch et al. and Orton et al. results. We also show the Noll et al. (1990) result which is a disk-averaged result based on high-resolution groundbased observations of the 5-μm spectrum made in 1994. Also shown is CIRS-based result of Fletcher et al. (2009a), which is an average of northern hemisphere latitudes from 10°N to 70°N. The latter two have error estimates, although there is considerable uncertainty as to how these results might differ if the authors had chosen different He/H<sub>2</sub> ratios in conducting their analyses. If taken at face value, these results suggest that the deep PH<sub>3</sub> mixing ratio is not likely to be as low as seems to be required to match our VIMS results for He/H<sub>2</sub> ratios below ~0.045. The results are quite different for arsine.

## 7.2. Limits to arsine adjustments

Arsine measurements are plotted in the lower panel of Fig. 21. Bezdard et al. (1989) derived AsH<sub>3</sub> mixing ratios of  $2.4^{+1.4}_{-1.2}$  ppb for the thermal component and  $0.39^{+0.21}_{-0.13}$  ppb for the reflected solar component. The latter is probably representative of the effective value in the 200 – 400 mbar range where they inferred a haze layer, while the former applies to the deep mixing ratio. Because we are using spectra with exceptionally high thermal emission values, the reflected solar contribution at thermal emission wavelengths is not very im-



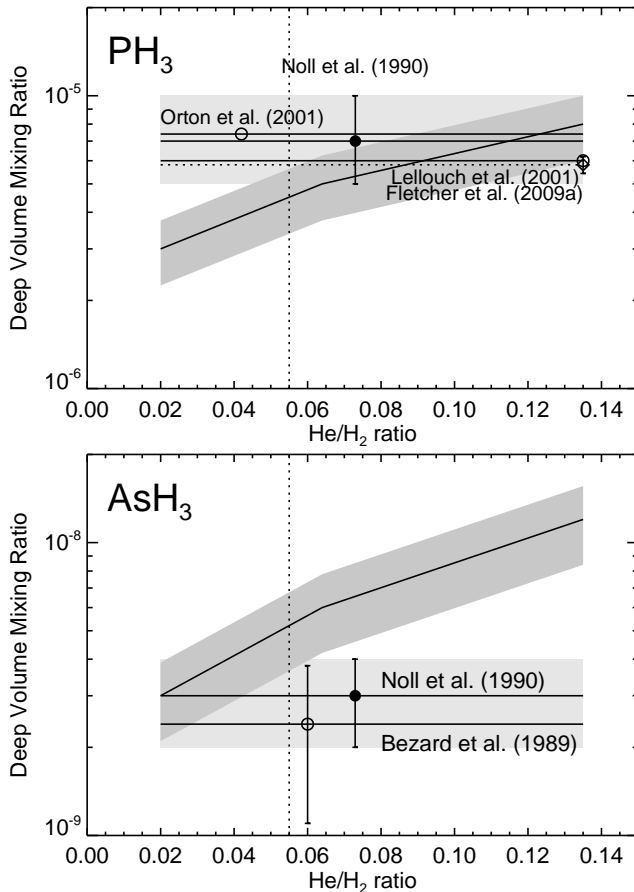


FIG. 21.— Deep mixing ratios of  $\text{PH}_3$  and  $\text{AsH}_3$  as a function of the  $\text{He}/\text{H}_2$  ratio. Solid curves with darker gray uncertainty bands are from our analysis of the brightest wake spectrum assuming that there is no deep absorbing cloud. Independent observations of  $\text{PH}_3$  and  $\text{AsH}_3$  provide possible limits on the  $\text{He}/\text{H}_2$  ratios. The independent values for  $\text{PH}_3$  and  $\text{AsH}_3$  are plotted at the  $\text{He}/\text{H}_2$  ratio that was used in each analysis. It is not clear how much a given analysis would change if a different  $\text{He}/\text{H}_2$  ratio had been assumed. The vertical dotted lines are plotted at a  $\text{He}/\text{H}_2$  ratio of 0.055, which is a possible compromise that crudely satisfies both constraints. See the main text for further discussion.

portant. In addition, even at its absorption peak the two-way  $\tau = 1$  level for  $\text{AsH}_3$  is deeper than 1 bar. Thus it is only the deep mixing ratio that is of interest here. Noll et al. (1989) inferred a value of  $1.8^{+1.8}_{-0.8}$  ppb. These are more compatible with the values we derived from the lower values of the  $\text{He}/\text{H}_2$  ratio. As shown in Fig. 21, the independent constraints on arsine suggest that the  $\text{He}/\text{H}_2$  ratio should be less than 0.06, while constraints suggested by  $\text{PH}_3$  measurements suggest values higher than 0.045. The compromise value of 0.055 is plotted as the vertical dotted line in Fig. 21.

### 7.3. Limits to ammonia adjustments

Selected independent measurements of Saturn’s ammonia mixing ratio profile are shown in Fig. 18. Microwave observations provide sensitivity to the deep mixing ratio, and both de Pater and Massie (1985) and Briggs and Sackett (1989) are in good agreement on a value of 400 – 600 ppm. Briggs and Sackett (1989) also note a decline in the  $\text{NH}_3$  VMR at pressures less than 5 bars and a value of 70 – 110 ppm at 2 bars. This provides the basis for our sketched profile in Fig. 18. The 70 – 110 ppm estimate covers the pres-

sure range most relevant for modeling Saturn’s 5- $\mu\text{m}$  spectra. The CIRS-based results of Fletcher et al. (2011), shown as the dark gray bar in Fig. 18, are closer to the profiles we used for the  $\text{He}/\text{H}_2$  ratio of 0.064, which is from (Prinn et al. 1984) and shown as the dashed curve. The nearby solid curve has the same deep mixing ratio, but follows the saturated vapor profile above the saturation level. The dot-dash curve traces the profile we used to suppress thermal emission in the model for  $\text{He}/\text{H}_2 = 0.135$ . This is well above the global average values measured in the 2 – 3 bar range, and is perhaps the strongest argument against a  $\text{He}/\text{H}_2$  ratio much greater than 0.06, at least under the assumption that the clearest wake region does not contain a deep absorbing cloud. In a region of unusually high 5.1- $\mu\text{m}$  brightness it would indeed be implausible to have much higher than normal levels of ammonia vapor. The profile we used to raise the I/F at 5.1  $\mu\text{m}$  in the case of a  $\text{He}/\text{H}_2$  ratio of 0.02 is not plotted here because ammonia had to be reduced to negligible levels in that case. An upper bound for that case remains to be determined. It is not clear what an implausible level would be for ammonia in an unusually clear region. Downwelling motions of gas from above (lower pressure than) the 1 bar level could certainly depress the ammonia mixing ratio at deeper levels. An example of such an effect was observed by the Galileo probe that entered an unusually clear region in Jupiter’s atmosphere at the edge of a 5- $\mu\text{m}$  hot spot, where mixing ratios of several condensable gases were depressed by roughly an order of magnitude (Niemann et al. 1998), presumably by downwelling motions. Thus, a highly depressed ammonia abundance in what appear to be a Saturnian “hot band” is quite plausible. An order of magnitude depletion could be obtained by mixing gas downward from the 1 bar level or above (lower pressure). Also relevant are 2.2-cm emission measurements from May 2011 (Janssen et al. 2013; Laraia et al. 2013), which showed that the wake region was becoming “dried out” with respect to ammonia vapor, supporting the conclusion that a depletion of  $\text{NH}_3$  clouds might be occurring, contradicting the idea that the region might have greater than average amounts of ammonia. The main message from consideration of ammonia constraints is that low values of the  $\text{He}/\text{H}_2$  ratio are more plausible than high values.

## 8. SUMMARY AND CONCLUSIONS

The remarkably uniform and 5- $\mu\text{m}$  bright wake of Saturn’s Great Storm of 2010 – 2011 was investigated with the help of VIMS spectral images, using both reflected sunlight portions of the spectrum and that part dominated by thermal emission ( $\lambda > 4.5 \mu\text{m}$ ) to constrain vertical cloud structure. Our conclusions from this analysis can be summarized as follows.

1. The wake region began with widespread appearance of absorption near 3  $\mu\text{m}$ , was generally very dark at thermal emission wavelengths (near 5  $\mu\text{m}$ ), with exceptions of local regions that were brighter at 5  $\mu\text{m}$  than even before the beginning of the storm. The regions brightest near 5  $\mu\text{m}$  were near the anticyclone that developed along with the convective storm feature.
2. As time progressed the regions of high 5- $\mu\text{m}$  brightness expanded longitudinally beginning near the middle of the wake region, eventually expanding latitudinally to cover the entire band from 29°N to 39°N, and all longitudes. In addition, by December 2012, the band became remarkably uniform, with an RMS deviation over longitude of only 2% in I/F at 5.12  $\mu\text{m}$  in the middle of the

band, and had similar latitudinal uniformity from 30°N to 39°N over most longitudes.

3. Before the storm began, VIMS spectra at the storm latitudes could be well fit using model structure with mainly just two cloud layers. In the 190 – 570 mbar range we inferred an upper layer of conservative particles of unknown composition and about 5 – 6 optical depths, which scatter as spheres with refractive index of  $n = 1.4 + 0i$  and particle radii slightly less than  $1 \mu\text{m}$ . A second, deeper layer of partially absorbing cloud particles was needed to limit thermal emission. Assuming an arbitrary single-scattering albedo of 0.95, and a physically thin sheet cloud structure, we found that it needed to be near 1.5 bars and have an optical depth near 3.
4. Applying our two-cloud model to the clear regions of the wake over time we found that the upper layer optical depth dropped by almost a factor of two initially, then slowly grew over time. The more significant effect was on the lower cloud that dropped its optical depth initially by a factor of four, reaching a factor of five decrease in December 2012, reaching a minimum optical depth of 0.57.
5. While the above results indicate that the lower cloud never completely disappeared, the presence or absence of that cloud depends critically on the assumed value of the  $\text{He}/\text{H}_2$  ratio and on what is assumed for mixing ratios of  $\text{NH}_3$ ,  $\text{PH}_3$  and  $\text{AsH}_3$ . For high values of the  $\text{He}/\text{H}_2$  ratio, either a significant cloud is required in the cleared regions or a significant increase in absorbing gas mixing ratios is required. For values less than 0.064, the lower cloud is not required, but for very low  $\text{He}/\text{H}_2$  ratios the atmosphere becomes so cold that the observed 5- $\mu\text{m}$  emission cannot be reached without significant reductions in gas absorptions.
6. When we fit a one-cloud (upper cloud) model to the spectra for a range of  $\text{He}/\text{H}_2$  ratios, allowing the  $\text{PH}_3$  profile to vary by a scale factor, we found that the best fit was at a  $\text{He}/\text{H}_2$  ratio near 0.064 and a  $\text{PH}_3$  deep mixing ratio of 5 ppm. But, with more realistic adjustments of  $\text{PH}_3$  mixing ratios at just the higher pressures, and also including adjustments of  $\text{NH}_3$  and  $\text{AsH}_3$ , we were able to expand the range of viable  $\text{He}/\text{H}_2$  ratios.
7. To limit the range of plausible  $\text{He}/\text{H}_2$  ratios, we compared our adjusted gas profiles to independent measurements of those profiles, finding that  $\text{PH}_3$  observations suggest that the  $\text{He}/\text{H}_2$  ratio should be greater than 0.05, while  $\text{AsH}_3$  observations suggest that the  $\text{He}/\text{H}_2$  ratio should be less than 0.06. A compromise value is 0.055. Ammonia limits suggest that the  $\text{He}/\text{H}_2$  ratio should be less than 0.07 and greater than 0.02.
8. Another factor is how well the various options fit the observed spectra. The best overall fit in the 4.5 – 5.15  $\mu\text{m}$  region was obtained with  $\text{He}/\text{H}_2 = 0.02$ , although that fit suppresses small spectral features below the

level observed, while the fit with  $\text{He}/\text{H}_2 = 0.135$  exaggerates those features and also produces a much worse overall fit, suggesting that a  $\text{He}/\text{H}_2 \sim 0.064$  is a better choice. The best fits in the 2.1- $\mu\text{m}$  region are obtained with  $\text{He}/\text{H}_2 = 0.02 - 0.064$ . In the net, fit quality favors  $\text{He}/\text{H}_2$  values in the 0.02 – 0.064 range.

9. If the broad clearing of the wake region is to be explained as a complete disappearance of lower cloud particles, and considering fit quality and all the independent constraints on absorbing gases, it appears that the  $\text{He}/\text{H}_2$  ratio would need to be in the range of  $0.055^{+0.10}_{-0.15}$ .
10. We also showed that including reflected sunlight in the 4.1 – 4.5  $\mu\text{m}$   $\text{PH}_3$  absorption band enabled VIMS observations to provide strong constraints on the  $\text{PH}_3$  mixing ratio in the 100 – 1000 mbar region. Our results in this region are roughly consistent with CIRS-based results of Fletcher et al. (2009a), but disagree strongly with VIMS-based results of Fletcher et al. (2011), by orders of magnitude in the 500 mbar region, where their deep pressure break-point and small scale height lead to much less  $\text{PH}_3$ . Our scale height ratio to the pressure scale height, valid for the entire range of  $\text{He}/\text{H}_2$  values we considered was in the range of 0.5 – 0.6, compared to values  $\sim 0.2$  for Fletcher et al. (2011). To allow for a sharper photochemical cutoff above 100 mbar, we needed to increase the scale height even further to compensate for lost absorption above that level, leading to a profile similar to that inferred by Lellouch et al. (2001), except for a somewhat lower upper break-point pressure.
11. We identified spectral regions where persistent discrepancies between model and observed spectra suggest the possibility of missing or erroneous information in the trace gas line data. As indicated in Fig. 19, the depth of the 4.74- $\mu\text{m}$  absorption feature in models always exceeds the measured depth, and there is a small spectral absorption feature near 4.85  $\mu\text{m}$  in the measured spectrum that is completely absent from model spectra. Also, as indicated in Fig. 20, the large 4.3- $\mu\text{m}$  absorption feature is more asymmetric in models than in VIMS measurements, with models producing less absorption on the long wavelength side of the absorption maximum.

It remains to be seen how long it will take for the wake region to return to the same state it had before the Great Storm began, or to return to a state of reduced 5- $\mu\text{m}$  emission. The wake remained relatively uniform and bright at 5  $\mu\text{m}$  into 2015, although some dimming seems to be underway (Momary et al. 2015). Analysis of its long term evolution beyond 2012 is left for future work.

#### ACKNOWLEDGMENTS.

Support for this work was provided by NASA through its Cassini Data Analysis and Participating Scientists (CDAPS) Program under grant NNX15AL10G. We thank Don Banfield and an anonymous reviewer for their attention to detail and for providing many useful suggestions that improved the manuscript.

## REFERENCES

- Anderson, J. A., Sides, S. C., Soltesz, D. L., Sucharski, T. L., Becker, K. J., 2004. Modernization of the Integrated Software for Imagers and Spectrometers. In: Mackwell, S., Stansbery, E. (Eds.), *Lunar and Planetary Science Conference*. Vol. 35 of *Lunar and Planetary Science Conference*. p. 2039.
- Bezard, B., Drossart, P., Lellouch, E., Tarrago, G., Maillard, J. P., 1989. Detection of arsine in Saturn. *Astrophys. J.* 346, 509–513.
- Borysow, A., 1991. Modeling of collision-induced infrared absorption spectra of H<sub>2</sub>-H<sub>2</sub> pairs in the fundamental band at temperatures from 20 to 300 K. *Icarus* 92, 273–279.
- Borysow, A., 1992. New model of collision-induced infrared absorption spectra of H<sub>2</sub>-He pairs in the 2-2.5 micron range at temperatures from 20 to 300 K - an update. *Icarus* 96, 169–175.
- Borysow, A., 1993. Erratum. *Icarus* 106, 614.
- Bowles, N., Calcutt, S., Irwin, P., Temple, J., 2008. Band parameters for self-broadened ammonia gas in the range 0.74 to 5.24  $\mu\text{m}$  to support measurements of the atmosphere of the planet Jupiter. *Icarus* 196, 612–624.
- Briggs, F. H., Sackett, P. D., 1989. Radio observations of Saturn as a probe of its atmosphere and cloud structure. *Icarus* 80, 77–103.
- Brown, R. H., Baines, K. H., Bellucci, G., Bibring, J.-P., Buratti, B. J., Capaccioni, F., Ceroni, P., Clark, R. N., Coradini, A., Cruikshank, D. P., Drossart, P., Formisano, V., Jaumann, R., Langevin, Y., Matson, D. L., McCord, T. B., Mennella, V., Miller, E., Nelson, R. M., Nicholson, P. D., Sicardy, B., Sotin, C., 2004. The Cassini Visual and Infrared Mapping Spectrometer (VIMS) Investigation. *Space Sci. Rev.* 115, 111–168.
- Butler, R. A. H., Sagui, L., Kleiner, I., Brown, L. R., 2006. The absorption spectrum of phosphine (PH<sub>3</sub>) between 2.8 and 3.7  $\mu\text{m}$ : Line positions, intensities, and assignments. *J. of Molec. Spectrosc.* 238, 178–192.
- Clark, R. N., Cruikshank, D. P., Jaumann, R., Brown, R. H., Stephan, K., Dalle Ore, C. M., Eric Livo, K., Pearson, N., Curchin, J. M., Hoefen, T. M., Buratti, B. J., Filacchione, G., Baines, K. H., Nicholson, P. D., 2012. The surface composition of Iapetus: Mapping results from Cassini VIMS. *Icarus* 218, 831–860.
- Conrath, B. J., Gautier, D., 2000. Saturn Helium Abundance: A Reanalysis of Voyager Measurements. *Icarus* 144, 124–134.
- Conrath, B. J., Gautier, D., Hanel, R. A., Hornstein, J. S., 1984. The helium abundance of Saturn from Voyager measurements. *Astrophys. J.* 282, 807–815.
- Courtin, R., Gautier, D., Marten, A., Bézard, B., Hanel, R., 1984. The composition of Saturn's atmosphere at northern temperate latitudes from Voyager IRIS spectra - NH<sub>3</sub>, PH<sub>3</sub>, C<sub>2</sub>H<sub>2</sub>, C<sub>2</sub>H<sub>6</sub>, CH<sub>3</sub>D, CH<sub>4</sub>, and the Saturnian D/H isotopic ratio. *Astrophys. J.* 287, 899–916.
- de Pater, I., Massie, S. T., 1985. Models of the millimeter-centimeter spectra of the giant planets. *Icarus* 62, 143–171.
- Dyudina, U. A., Ingersoll, A. P., Ewald, S. P., Porco, C. C., Fischer, G., Yair, Y., 2013. Saturn's visible lightning, its radio emissions, and the structure of the 2009-2011 lightning storms. *Icarus* 226, 1020–1037.
- Fischer, G., Kurth, W. S., Gurnett, D. A., Zarka, P., Dyudina, U. A., Ingersoll, A. P., Ewald, S. P., Porco, C. C., Wesley, A., Go, C., Delcroix, M., 2011. A giant thunderstorm on Saturn. *Nature* 475, 75–77.
- Fletcher, L. N., Baines, K. H., Momary, T. M., Showman, A. S., Irwin, P. G. J., Orton, G. S., M., R., Merlit, C., 2011. Saturn's tropospheric composition and clouds from Cassini/VIMS 4.6 – 5.1  $\mu\text{m}$  nightside spectroscopy. *Icarus* 214, 510–533.
- Fletcher, L. N., Orton, G. S., Teanby, N. A., Irwin, P. G. J., 2009a. Phosphine on Jupiter and Saturn from Cassini/CIRS. *Icarus* 202, 543–564.
- Fletcher, L. N., Orton, G. S., Teanby, N. A., Irwin, P. G. J., Bjoraker, G. L., 2009b. Methane and its isotopologues on Saturn from Cassini/CIRS observations. *Icarus* 199, 351–367.
- Fouchet, T., Moses, J. I., Conrath, B. J., 2009. Saturn: Composition and Chemistry. In: Dougherty, M. K., Esposito, L. W., Krimigis, S. M. (Eds.), *Saturn from Cassini-Huygens*. Springer, Dordrecht, Heidelberg, London, New York, pp. 83–112.
- Fry, P. M., Sromovsky, L. A., 2014. Computation of Concentric Shell Particle Scattering Effects in Jovian Clouds. Vol. 46 of *AAS/Division for Planetary Sciences Meeting Abstracts*, #422.20.
- Gautier, D., Conrath, B., Flasar, M., Achterberg, R., Schinder, P., Kliore, A., Cassini Cirs, Radio Science Teams, 2006. The helium to hydrogen ratio in Saturn's atmosphere from Cassini CIRS and radio science measurement. In: 36th COSPAR Scientific Assembly. Vol. 36 of *COSPAR Meeting*. p. 867.
- Gautier, D., Conrath, B., Flasar, M., Hanel, R., Kunde, V., Chedin, A., Scott, N., 1981. The helium abundance of Jupiter from Voyager. *J. Geophys. Res.* 86, 8713–8720.
- Hanel, R., Conrath, B., Flasar, F. M., Kunde, V., Maguire, W., Pearl, J. C., Pirraglia, J., Samuelson, R., Herath, L., Allison, M., Cruikshank, D. P., Gautier, D., Gierasch, P. J., Horn, L., Koppany, R., Ponnampuruma, C., 1981. Infrared observations of the Saturnian system from Voyager 1. *Science* 212, 192–200.
- Hansen, J. E., Travis, L. D., 1974. Light scattering in planetary atmospheres. *Space Sci. Rev.* 16, 527–610.
- Janssen, M. A., Ingersoll, A. P., Allison, M. D., Gulkis, S., Laraia, A. L., Baines, K. H., Edgington, S. G., Anderson, Y. Z., Kelleher, K., Oyafuso, F. A., 2013. Saturn's thermal emission at 2.2-cm wavelength as imaged by the Cassini RADAR radiometer. *Icarus* 226, 522–535.
- Lacis, A. A., Oinas, V., 1991. A description of the correlated-k distribution method for modelling nongray gaseous absorption, thermal emission, and multiple scattering in vertically inhomogeneous atmospheres. *J. Geophys. Res.* 96, 9027–9064.
- Laraia, A. L., Ingersoll, A. P., Janssen, M. A., Gulkis, S., Oyafuso, F., Allison, M., 2013. Analysis of Saturn's thermal emission at 2.2-cm wavelength: Spatial distribution of ammonia vapor. *Icarus* 226, 641–654.
- Lellouch, E., Bézard, B., Fouchet, T., Feuchtgruber, H., Encrenaz, T., de Graauw, T., 2001. The deuterium abundance in Jupiter and Saturn from ISO-SWS observations. *Astron. & Astrophys.* 370, 610–622.
- Li, C., Ingersoll, A. P., 2015. Moist convection in hydrogen atmospheres and the frequency of Saturn's giant storms. *Nature Geoscience* 8, 398–403.
- Lindal, G. F., Sweetnam, D. N., Eshleman, V. R., 1985. The atmosphere of Saturn - an analysis of the Voyager radio occultation measurements. *Astron. J.* 90, 1136–1146.
- McCord, T. B., Coradini, A., Hibbitts, C. A., Capaccioni, F., Hansen, G. B., Filacchione, G., Clark, R. N., Ceroni, P., Brown, R. H., Baines, K. H., Bellucci, G., Bibring, J.-P., Buratti, B. J., Bussoletti, E., Combes, M., Cruikshank, D. P., Drossart, P., Formisano, V., Jaumann, R., Langevin, Y., Matson, D. L., Nelson, R. M., Nicholson, P. D., Sicardy, B., Sotin, C., 2004. Cassini VIMS observations of the Galilean satellites including the VIMS calibration procedure. *Icarus* 172, 104–126.
- Miller, E. A., Klein, G., Juergens, D. W., Mehaffey, K., Oseas, J. M., Garcia, R. A., Giandomenico, A., Irigoyen, R. E., Hickok, R., Rosing, D., Sobel, H. R., Bruce, C. F., Flamini, E., Devidi, R., Reininger, F. M., Dami, M., Soufflot, A., Langevin, Y., Huntzinger, G., 1996. The Visual and Infrared Mapping Spectrometer for Cassini. In: Horn, L. (Ed.), *Society of Photo-Optical Instrumentation Engineers (SPIE) Conference Series*. Vol. 2803 of *Society of Photo-Optical Instrumentation Engineers (SPIE) Conference Series*. pp. 206–220.
- Momary, T. W., Baines, K. H., 2014. The Anticyclonic Eye of the Storm: Evolution of Saturn's Great Storm Region and Associated Anticyclone as seen by Cassini/VIMS. In: *AAS/Division for Planetary Sciences Meeting Abstracts*. Vol. 46 of *AAS/Division for Planetary Sciences Meeting Abstracts*. p. #422.11.
- Momary, T. W., Baines, K. H., Badman, S., Brown, R. H., Buratti, B. J., Clark, R. N., Nicholson, P. D., Sotin, C., 2015. The Ongoing Evolution of a Long-Lived Anticyclone in Saturn's Great Storm Region as seen by Cassini/VIMS. Vol. 47 of *AAS/Division for Planetary Sciences Meeting Abstracts*, #311.19.
- Niemann, H. B., Atreya, S. K., Carignan, G. R., Donahue, T. M., Haberman, J. A., Harpold, D. N., Hartle, R. E., Hunten, D. M., Kasprzak, W. T., Mahaffy, P. R., Owen, T. C., Way, S. H., 1998. The composition of the Jovian atmosphere as determined by the Galileo probe mass spectrometer. *J. Geophys. Res.* 103, 22831–22846.
- Noll, K. S., Geballe, T. R., Knacke, R. F., 1989. Arsine in Saturn and Jupiter. *Astrophys. J. Lett.* 338, L71–L74.
- Noll, K. S., Larson, H. P., Geballe, T. R., 1990. The abundance of AsH<sub>3</sub> in Jupiter. *Icarus* 83, 494–499.
- Orton, G. S., Ingersoll, A. P., 1980. Saturn's atmospheric temperature structure and heat budget. *J. Geophys. Res.* 85, 5871–5881.
- Orton, G. S., Serabyn, E., Lee, Y. T., 2000. Vertical distribution of PH<sub>3</sub> in Saturn from observations of its 1-0 and 3-2 rotational lines. *Icarus* 146, 48–59.
- Orton, G. S., Serabyn, E., Lee, Y. T., 2001. Erratum, Volume 146, Number 1, pages 48-59 (2000), in the article "Vertical Distribution of PH<sub>3</sub> in Saturn from Observations of Its 1-0 and 3-2 Rotational Lines." *Icarus* 149, 489–490.
- Prinn, R. G., Larson, H. P., Caldwell, J. J., Gautier, D., 1984. Composition and chemistry of Saturn's atmosphere. In: Gehrels, T. & Matthews, M. S. (Ed.), *Saturn*. Univ. of Arizona Press, Tucson, pp. 88–149.

- Rothman, L. S., Gordon, I. E., Barbe, A., Benner, D. C., Bernath, P. F., Birk, M., Boudon, V., Brown, L. R., Campargue, A., Champion, J., Chance, K., Coudert, L. H., Dana, V., Devi, V. M., Fally, S., Flaud, J., Gamache, R. R., Goldman, A., Jacquemart, D., Kleiner, I., Lacome, N., Lafferty, W. J., Mandin, J., Massie, S. T., Mikhailenko, S. N., Miller, C. E., Moazzen-Ahmadi, N., Naumenko, O. V., Nikitin, A. V., Orphal, J., Perevalov, V. I., Perrin, A., Predoi-Cross, A., Rinsland, C. P., Rotger, M., Šimečková, M., Smith, M. A. H., Sung, K., Tashkun, S. A., Tennyson, J., Toth, R. A., Vandaele, A. C., Vander Auwera, J., 2009. The HITRAN 2008 molecular spectroscopic database. *J. Quant. Spectrosc. & Rad. Transf.* 110, 533–572.
- Sánchez-Lavega, A., del Río-Gaztelurrutia, T., Delcroix, M., Legarreta, J. J., Gómez-Forrellad, J. M., Hueso, R., García-Melendo, E., Pérez-Hoyos, S., Barrado-Navascués, D., Lillo, J., International Outer Planet Watch Team IOPW-PVOL, 2012. Ground-based observations of the long-term evolution and death of Saturn's 2010 Great White Spot. *Icarus* 220, 561–576.
- Sayanagi, K. M., Dyudina, U. A., Ewald, S. P., Fischer, G., Ingersoll, A. P., Kurth, W. S., Muro, G. D., Porco, C. C., West, R. A., 2013. Dynamics of Saturn's great storm of 2010-2011 from Cassini ISS and RPWS. *Icarus* 223, 460–478.
- Sromovsky, L. A., Baines, K. H., Fry, P., 2013. Saturn's Great Storm of 2010-2011: Evidence for ammonia and water ices from analysis of VIMS spectra. *Icarus* 226, 402–418.
- Sromovsky, L. A., Fry, P. M., 2010. The source of 3- $\mu\text{m}$  absorption in Jupiter's clouds: Reanalysis of ISO observations using new  $\text{NH}_3$  absorption models. *Icarus* 210, 211–229.
- Sromovsky, L. A., Fry, P. M., Boudon, V., Campargue, A., Nikitin, A., 2012. Comparison of line-by-line and band models of near-IR methane absorption applied to outer planet atmospheres. *Icarus* 218, 1–23.
- Tarrago, G., 1996. Ground state rotational energies of arsine. *J. of Mol. Spectr.* 178, 10–21.
- Tyler, G. L., Eshleman, V. R., Anderson, J. D., Levy, G. S., Lindal, G. F., Wood, G. E., Croft, T. A., 1982. Radio science with Voyager 2 at Saturn - Atmosphere and ionosphere and the masses of Mimas, Tethys, and Iapetus. *Science* 215, 553–558.
- von Zahn, U., Hunten, D. M., Lehmann, G., 1998. Helium in Jupiter's atmosphere: Results from the Galileo probe helium interferometer experiment. *J. Geophys. Res.* 103, 22815–22830.
- Zheng, C., Borysow, A., 1995. Modeling of collision-induced infrared absorption spectra of  $\text{H}_2$  pairs in the first overtone band at temperatures from 20 to 500 K. *Icarus* 113, 84–90.